

NEUTRON SCATTERING OF PARENT AND REDUCED GRAPHENE OXIDES

Elena F. Sheka¹ and Ireneusz Natkaniec^{2,3}

¹Department of Theoretical Physics and Mechanics, Peoples' Friendship University of Russia, Moscow, Russia

²Faculty of Physics, Adam Mickiewicz University, 61-614, Poznań, Poland

³Frank Laboratory of Neutron Physics, Joint Institute for Nuclear Research, 141980, Dubna, Russia

Received: August 20, 2015

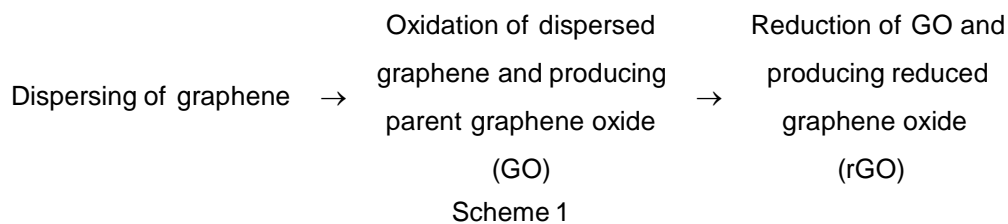
Abstract. The current paper summarizes results of an extended neutron scattering study of a three-part set of parent and reduced graphene oxide (GO and rGO, respectively) of different origin. The first part concerned the rGO of natural origin presented by wet and dry shungite carbons [1,2], the second was related to synthetic GO and rGO with the latter produced in the course of chemical treatment [3], the third part presents another pair of synthetic GO/rGO products with the latter produced via thermo exfoliation of the parent GO [4]. The study involved both the neutron diffraction (ND) and inelastic neutron scattering (INS). The neutron diffraction patterns confirmed stacking structures of all the species consisting of a number of layers of nanosize (natural products) and microsize (synthetic products) lateral dimension and the interlayer distances of 7.0-7.2 Å and 3.4-3.5 Å for GO and rGO, respectively. One-phonon amplitude-weighted density of vibrational states $G(\omega)$ represents the inelastic incoherent neutron scattering spectra of the products. The obtained data are analyzed basing on calculated $G(\omega)$ functions. The performed study has convincingly shown that neutron scattering clearly distinguishes GO and rGO species and well exhibits both common features and differences related to the members of the two communities. If retained water in GOs and graphene-hydride nature of rGOs provide the commonality of dynamic properties within each of the community, the difference in the relevant sheet topology is responsible for a noticeable variability of the latter. The study has convincingly shown a large polyvariance of both GO and rGO products evidencing their topochemical nature.

1. INTRODUCTION

As mentioned by K.Novoselov et al. [5], graphene modern technology can be divided into two independent domains, namely: 'low performance' (LP) and 'high performance' (HP) ones. The former includes a wide range of practical applications based on nanoscale graphene material. Products of the second domain based on a micro-size and larger single or multi-layer graphene sheets. This separation of the graphene technology into two types, held *de facto*, is not just a tribute to simplify operating with complex technologies, but, in fact, is a consequence of the nature of the graphene molecule-crys-

tal dualism and technical implementation of its unique chemical and physical properties [6], respectively. Both the successful implementation of any technology and the difficulties arising on this way depend primarily on the material in use. Serious problems associated with the development of processing methods aimed at the mass production of micro- and macro-dimension crystalline graphene sheet are objective reasons by postponing the implementation of the graphene HP technology up to 2030 [5,7]. The latter is further exacerbated by the very high cost of this material [8]. Realization of the LP technology proved more successful. Active efforts of numerous teams of chemists resulted in solving

Corresponding author: Elena F. Sheka, e-mail: sheka@icp.ac.ru



the problem of mass production of the necessary technological material - technical (molecular) graphene. This material is the final product of a complicated chemical-technological cycle, a concise description of which is presented by Scheme 1.

In all the many cases, structural analysis shows a pronounced non-planarity of GO sheets and nearly full recovery of the planarity of the basal plane of the carbon skeleton of rGO sheets, in connection with which thus produced rGO is often referred to as graphene.

Unlike hitherto used technological materials of strictly standardized chemical composition and structure, such a standardization of both GO and rGO products is not possible. The point is that the two terms refer to very wide range of substances, which actually represent various oxyhydride polyderivatives of graphene molecules of different chemical composition, size, and shape due to which the products can be characterized only by a restricted number of common features. Thus, in the GO case, there are two such characteristics that concern 1) interlayer distance between the GO sheets of $\geq 7 \text{ \AA}$ and 2) an average chemical composition described by the C:O~2:1 ratio. The former exhibits the fact that both basal plane and the circumference area of the parent graphene molecules are involved in the oxidation while the latter points to the prepotency of epoxy units among the GO oxygen-containing groups (OCGs). A common feature of rGO is related to the interlayer distance of $\sim 3.5 \text{ \AA}$ that points to the recovered planarity of the rGO carbon skeleton, on one hand, and to the location of residual OCGs in the circumference area [6,9], on the other. Individual differences within the two communities are caused by the difference in size and shape of carbon skeletons of the parent graphene molecules and, consequently, by different numbers of attached OCGs, as well as by evidently individual combinations of these groups in each case. These circumstances result in that the structure and chemical composition of both GO and rGO may change on each stage of their chemical synthesis. The high-degree polyvariance of the chemical composition and structure of synthesized GO and rGO are widely discussed in the literature

[10-13]. Thus, such an important parameter of rGOs produced in the different laboratories as the residual oxygen concentration can vary up to 20 times.

The property instability deprives the obtained synthetic products the requested technological stability and stimulates studies aimed at both disclosing the sources of instability and finding the way to produce reliable products. Up to date, the question of controlling both the GO and rGO chemical composition and size is the main motivation of numerous studies (see eg, Refs. [14] and [15]). Empirical solution of the former problem rests first of all in determination of C:O:H mass contents of the products. While the latter requires the application of a set of complementary techniques, such as XRF, TGA, Raman, and FTIR spectroscopy, XRD, XPS, REELS, and so forth, it is mainly focused on the evaluation of carbon and oxygen contents, leaving outside hydrogen among others small dopants. However, as was shown recently [1,2], the elucidation of the hydrogen role allows getting close the key question of chemical composition of both GO and rGO products. The quoted results were obtained by studying the scattering of thermal neutrons that is superb sensitive to protium. Once stimulated by the results obtained, the authors have suggested to extend the neutron scattering study over a set of synthetic GO and rGO products of different origin. As turned out, the performed study has allowed not only to reveal the retained water in GO and hydrogen-enriched carbon cores of rGO as new facets of the product structure and chemical composition, but also to show the way to link differences in the product behaviour with chemical protocols of their production as well as to shed light on the reasons of their instability in time.

Three sets of objects were studied. The first was the rGO one of natural origin presented by wet and dry shungite carbons [1,2], the second and the third ones presented pair of synthetic GO/rGO products - the latter produced either in the course of chemical treatment [3] or via thermo-exfoliation of the parent GO [4], respectively. The study involved both the neutron diffraction (ND) and inelastic neutron scattering (INS).

Table 1. Mass content in wt.% and chemical composition of GO and rGO products.

Products	C	O	H	Chemical formula per one benzoid unit	References
Shungite carbon	95.5±0.6	3.3±0.4	2.0-0.7	$C_6O_{0.1}H_{1.6-0.7}$	[20]
Ak-rGO	92.0±1.0	5.5±0.5	1.5±0.5	$C_6O_{0.3}H_{1.17}$	[22]
TErGO	87.1±0.3	12.1±0.3	0.5±0.3	$C_6O_{0.7}H_{0.36}$	[4]
Ak-GO	58.0±1.0	39.0±1.0	1.5±0.5	$C_6O_3H_{1.86}$	[22]
ppGO	56.2±0.3	40.5±0.3	0.7±0.3	$C_6O_3H_{0.85}$	[4]

2. METHODS IN USE

2.1. Samples

2.1.1. rGO of natural origin

As has been shown recently [16], deposits of shungite rocks present the natural pantry of nanoscale rGO (sh-rGO). The matter was presented in INS study by three powdered samples, namely: pristine shungite carbon Sh1 that was the natural raw material with C ≥ 95 wt.% from Shunga's de-

posits (*wet shungite*) [17], shungite Sh2, obtained when drying Sh1 at 110 °C for a week (*dry shungite*), and shungite Sh3 related to a solid condensate of colloids of the shungite Sh1 aqueous dispersions. Stored under ambient conditions, it presents another *wet shungite*. Both Sh1 and Sh3, sustained under ambient conditions for a long time, at soft vacuum and temperature above 100 °C, underwent releasing from the retained water constituting ~4% of the total mass. Raman scattering [17], high-resolution solid state ^{13}C NMR [18], and Auger spectroscopy

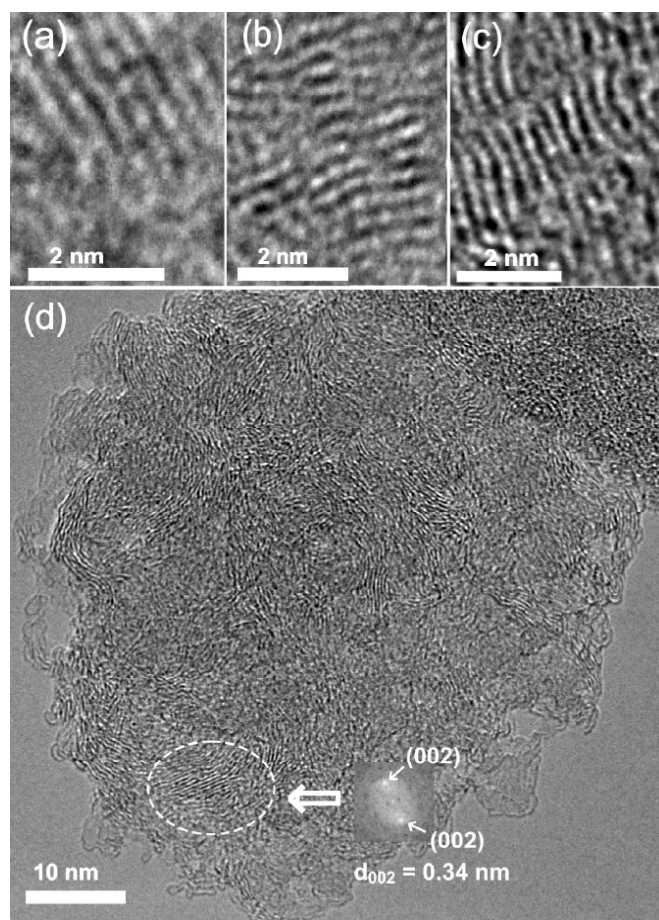


Fig. 1. HRTEM different scales in shungite carbon structure [20]: stacks of planar (a,b) and bent (c) rGO layers; general view of shungite particle (d). Insert shows the Fourier diffractogram related to the marked area.

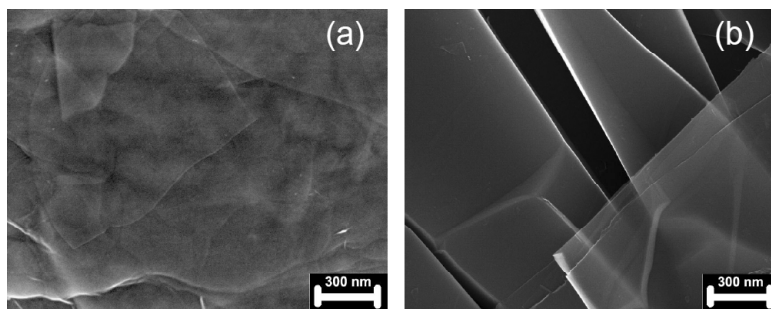


Fig. 2. SEM images of Ak-GO (a) and Ak-rGO (b) products (Zeiss SUPRA 40 Carl Zeiss MicroImaging GmbH), adapted from our paper [3].

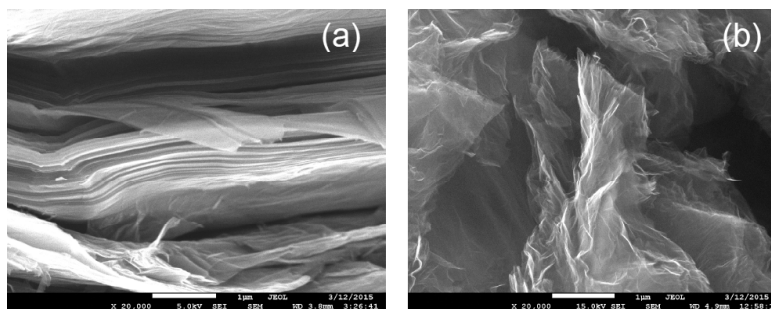


Fig. 3. SEM images of ppGO (a) and TErGO (b) (JSM7001F microscope). White bars mark the image scaling of 100 μm and 10 μm in (a) and (b) panels, respectively.

[19] show a deep similarity of shungites Sh1 and Sh3. The atomic chemical composition of the pristine shungite, determined by high resolved electron microscopy combined with the energy dispersive spectral (X-Ray) (EDS) analysis (C and O) and flash-combustion analysis (H) [20], is given in Table 1. Statistic dispersion is the largest for the hydrogen content due to which pristine shungite can be characterized by a stoichiometric composition $\text{C}_6\text{O}_{0.1}\text{H}_{1.6-0.7}$ per one benzenoid ring with a blurred hydrogen content. General characteristic view of the shungite structure is shown in Fig. 1.

2.1.2. Chemically produced products of the Akolab company

Akolab's products [21] are produced following three steps [22]. Step 1 concerns the fabrication of graphite oxide (GrO) performed by modified Hummers' method [23]. Step 2 is aimed at obtaining Ak-GO for which GrO was dispersed with ultrasound. The reduction of previously obtained Ak-GO during step 3 is performed in batch reactors at temperature and pressure over the critical parameters of isopropanol ($T_c = 234.9\text{ }^\circ\text{C}$, $P_c = 5.3\text{ MPa}$), which provides an effective hydrogenolysis of C-O and C=O bonds [24].

The atomic chemical composition of the products, determined by flash-combustion elemental analysis, is given in Table 1. The obtained data are confirmed by XPS study of the products. A stoichiometric

composition $\text{C}_6\text{O}_3\text{H}_{1.86}$ per one benzenoid ring is characteristic of Ak-GO while $\text{C}_6\text{O}_{0.3}\text{H}_{1.17}$ should be attributed to Ak-rGO. Evidently, due to planarization of the related Ak-rGO fragments, hydrogen and oxygen atoms occupy not the basal plane of the units but are accommodated in the circumference pointing to the oxyhydride origin of the framing area of the synthetic rGO. SEM images of the products are shown in Fig. 2.

2.1.3. Chemically produced GO paper and thermally exfoliated rGO

The parent GO was obtained as GO paper (ppGO below) from oxidized graphite (GrO) in the course of a repetitive dispersing of GrO in HCl (1%) solution [4]. A general appearance of the ppGO is presented in Fig. 3a. Thermal shock is used to produce exfoliation and/or reduction of GO [25]. This type of thermal treating initiates exothermal reactions of the decomposition of OCGs that is accompanied by expansion due to evolved gases and production of thermally exfoliated reduced graphene oxide (TErGO). A general appearance of the TErGO is presented in Fig. 3b.

The element content of both ppGO and TErGO was determined by flash-combustion elemental analysis and gaseous volumetry. The latter monitors yields of gaseous products (CO_2 , CO, H_2O , and other) under stepwise annealing of the samples at

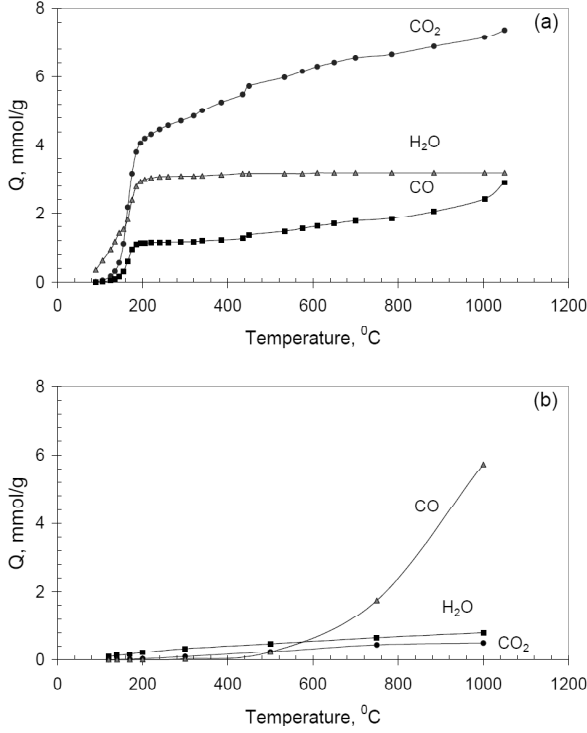


Fig. 4. Temperature dependence of the evolved gases yields Q at stepwise annealing of ppGO (a) and TErGO (b). Presumably, the contact of highly active TErGO with air is mainly responsible for the oxygen content, adapted from our paper [4].

different temperature. Typical temperature dependences of the measured yields for ppGO and TErGO samples are presented in Fig. 4. The accuracy of each element determination was about 0.30 wt.% in both cases. Table 1 summarizes data on mass content of the studied samples. A stoichiometric composition $\text{C}_6\text{O}_3\text{H}_{0.85}$ per one benzenoid ring can be attributed to ppGO while TErGO is well described by the $\text{C}_6\text{O}_{0.7}\text{H}_{0.36}$ formula.

Powdered spectral graphite of 99.9999% chemical purity was used to register both the reference NPD and INS spectrum from pure carbon material in all the cases.

2.2. Neutron scattering experiments

The neutron scattering study was performed at the high flux pulsed IBR-2 reactor of the Frank Laboratory of Neutron Physics at the Joint Institute for Nuclear Research by using the inverted-geometry time-of-flight (TOF) spectrometer NERA [26]. The investigated samples are illuminated by white neutron beam analyzed by time-of-flight method on the 110 m flight path from the IBR-2 moderator to the sample. The NERA spectrometer allows for simultaneous recording of both neutron powder diffrac-

tion (NPD) and inelastic neutron scattering (INS) spectra. The NPD spectra were obtained for a few scattering angles of diffraction detectors to provide measuring of different inter-planar distances with a comparable accuracy. The INS spectra were collected at the final energy of the scattered neutrons fixed by beryllium filters and crystal analyzers at $E_f = 4.65$ meV, over fifteen scattering angles from 20° to 160° followed in 10° . The experiments were performed at low and room temperatures.

2.3. Theoretical background

Experimentally, differential cross-section is the measure of the INS intensity. It consists of two parts

$$\frac{d^2 \sigma}{d\Omega dE} = \left(\frac{d^2 \sigma}{d\Omega dE} \right)_{coh} + \left(\frac{d^2 \sigma}{d\Omega dE} \right)_{inc} \propto \sum_n \frac{(b_n^{coh})^2}{M_n} S_n^{coh}(Q, \omega) + \sum_n \frac{(b_n^{inc})^2}{M_n} S_n^{inc}(Q, \omega), \quad (1)$$

which present coherent (*coh*) and incoherent (*inc*) INS [27]. Lengths of neutron scattering, b_n^{coh} and b_n^{inc} , as well as mass of the n -th nucleus M_n , different for atoms and isotopes of the same atoms, determine the contribution of each nucleus into the total INS intensity. The presence of hydrogen isotope H^1 in the studied samples, for which b_n^{inc} exceeds both b_n^{coh} and b_n^{inc} of other nuclei by several times, gives the right to limit itself to the contribution of the second member of Eq. (1), presenting inelastic incoherent neutron scattering (IINS), into the scattering cross-section when evaluating the INS spectra intensity. In the framework of commonly used inelastic incoherent one-phonon scattering approximation it is expressed as [27]

$$\sigma_1^{inc}(E_i, E_f, \varphi, T) \approx \sqrt{\frac{E_f}{E_i}} \frac{\hbar |Q(E_i, E_f, \varphi)|^2}{\omega} \times \sum_n \frac{(b_n^{inc})^2}{M_n} \frac{\exp(-2W_n)}{1 - \exp\left(-\frac{\hbar\omega}{k_B T}\right)} G_n(\omega). \quad (2)$$

Here, $Q(E_i, E_f, \varphi)$ is the neutron momentum transfer; $\omega = (E_i - E_f)$, is the neutron energy transfer; $\exp(-2W_n)$ is the Debye-Waller factor; $G_n(\omega)$ presents the n -th atom contribution into the amplitude-weighted density of vibrational states (AWDVS)

$$G_n(\omega) = \sum_j [A_j^n(\omega)]^2 \delta(\omega - \omega_j). \quad (3)$$

Here, $A_j^n(\omega)$ is the amplitude of the n -th atom displacement in the eigenvector of the j -th phonon mode ω_j . If the matter consists of different nuclei, each nuclear family of the k -th type superpositionally enters the total scattering intensity with weighting factors F_k given as

$$F_k(\omega) = \sum_{n_k} \frac{(b_{n_k}^{inc})^2}{M_{n_k}} \exp(-2W_{n_k}) G_{n_k}(\omega). \quad (4)$$

Here summation is extended over the atomic nuclei belonging to the k -th family. Accordingly, Eq. (2) can be rewritten as

$$\sigma_1^{inc}(E_i, E_f, \varphi, T) \approx \sqrt{\frac{E_f}{E_i}} \frac{\hbar |Q(E_i, E_f, \varphi)|^2}{\omega} \frac{\sum_k F_k(\omega)}{1 - \exp\left(-\frac{\hbar\omega}{k_B T}\right)} \quad (5)$$

Evidently, $b_{n_k}^{inc}$, M_{n_k} , and $A_j^n(\omega)$ are the main parameters that determine the weighting factors F_k . In the case of GO and rGO products the nuclear families are presented by H¹, C¹², and O¹⁶ isotopes. Incoherent scattering lengths of C¹² and O¹⁶ are zero due to which the isotopes do not scatter incoherently in contrast to H¹ for which $b_n = 25.274$ fm. However, the ability of C¹² and O¹⁶ to scatter coherently provides their contribution into the total INS spectra due to the first member in Eq. (1). Similarly to the incoherent case, the coherent scattering contribution is determined by $(b_n^{coh})^2/M_n$ factors where b_n^{coh} constitute 6.65 fm and 5.8 fm for C¹² and O¹⁶ isotopes, respectively. Taking together, the maximum contributions of H¹, C¹², and O¹⁶ nuclei form a series 639:3.7:2.1 thus showing that under equal conditions scattering from protium atoms are 173 and 304 times stronger than that from carbon and oxygen atoms, respectively. This allows neglecting the contribution of both heavy atom families into the total scattering intensity thus presenting $F(\omega) = \sum_k F_k(\omega)$ as a mononuclear quantity

$$G(\omega) = \sum_n G_n(\omega) \quad (6)$$

that is the hydrogen-partitioned AWDVS. Calculations of the AWDVS $G(\omega)$ spectra were performed in the frame work of molecular density functional theory. Details of the calculations are given elsewhere [28].

The inaccuracy caused by this approximation is illustrated by the data shown in Fig. 5. The model chosen for calculations presents a graphene hydride molecule C₆₆H₂₂ that will be discussed in Section

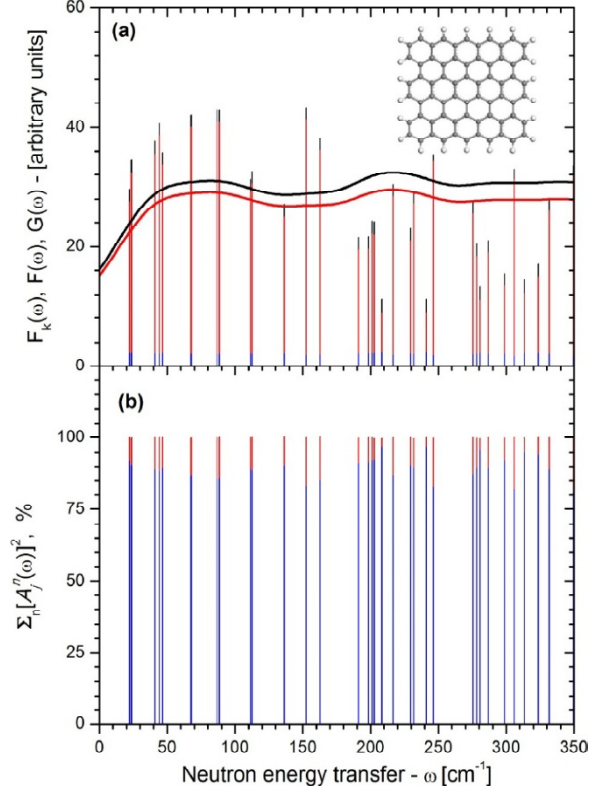


Fig. 5. Quantitative evaluation of the accuracy of the AWDVS approximation and ‘riding effect’ related to graphite-like vibrational modes (see text). Blue and red bars mark the contribution of carbon and hydrogen atoms, respectively. Insert presents C₆₆H₂₂ molecule.

4.1.2 in details. Values $|A_j^n(\omega)|^2$ in Fig. 5b are summarized over carbon (blue bars) and hydrogen (red bars) atoms for each vibrational j -mode provided that $\sum_n |A_j^n(\omega)|^2 = 1$ (100%). Blue and red bars in Fig. 5a present partitioned contributions $F_k(\omega)$ of carbon and hydrogen atoms into the total $F(\omega)$ spectrum (black bars), respectively; red and black curves are related to $G(\omega)$ and $F(\omega)$ spectra convoluted by using Lorentzians of 80 cm⁻¹ half width.

As seen in Fig. 5b, vibrational modes in the chosen frequency interval are mainly provided by carbon atoms and the contribution of hydrogen atoms into each of the modes does not exceed 10%. Therefore, the data presented in the figure are related to the case that is the most unfavorable for the neutron scattering from the considered molecule. At the same time, the hydrogen atoms contribution, expressed by $G(\omega)$, into the total scattering intensity $F(\omega)$ in Fig. 5a dominates and constitutes more than 90% due to which the inaccuracy in substituting $F(\omega)$ to $G(\omega)$ does not exceed 10%. When the hydrogen atom contribution into vibrational modes increases the inaccuracy evidently becomes less.

Besides the inaccuracy problem, the data in Fig. 5 exhibit a very important effect related to the neutron spectroscopy of hydrogen-containing objects and known as ‘riding effect’ (see [29] and references therein). The latter is a result of a peculiar sensitization of heavy atom vibrations with respect to neutron scattering by small contribution of hydrogen atom displacements in the relevant vibrational modes.

3. NEUTRON SCATTERING EXPERIMENT

3.1. Neutron powder diffraction

3.1.1. Shungite carbon

A set of NPD plottings for the three shungite carbons at 20K is presented in Fig. 6a. The data are related to samples in aluminum sample holder and cryostat due to which the plottings are overloaded with Al(hkl) reflections. Exempted from the Al reflections and corrected for background inelastic scattering, NDP plottings of Sh1 and Sh2 are presented in Fig. 6b. Similarly to the reference graphite spectrum, given at the bottom, the main features of the shungite diffractograms concern peaks related to Gr(002), Gr(100), and Gr(110) reflections all of which are broadened and upshifted. As seen in the figure, the narrow Gr(002) peak of graphite, the shape and width of which correspond to the resolution function of spectrometer and whose position determines d_{002} interfacial distance between the neighboring graphite layers, is substituted with broad peaks whose characteristics are given in Table 2. The positions of peak’s maxima, A_{002} , and the relevant FWHMs, B_{002} , were determined by the Gauss fitting procedure. Slight upshift of the shungite peaks convincingly evidences the conservation of graphite-like structure of all the samples, while the peak wide broadening tells about a considerable space restriction. The latter is usually attributed to the narrowing of the coherent scattering region (CSR) of scatterers. According to widely used Scherrer’s equation, the FWHM of a diffraction peak B and the CSR length L_{CSR} are inversely connected: $B = k\lambda/L_{CSR}\sin\Theta$, where k is a fitting factor, λ and Θ are the neutron wave length and scattering angle. When the diffraction study is performed for a set of samples under the same conditions, it is possible to take one of the samples as the reference and to determine L_{CSR} of the remaining samples addressing to that of the reference. In the current study, L_{CSR}^{ref} is attributed to crystalline graphite and constitutes ~ 20 nm along c direction [30]. Therefore, L_{CSR}^c of the studied shungite carbons can be determined as

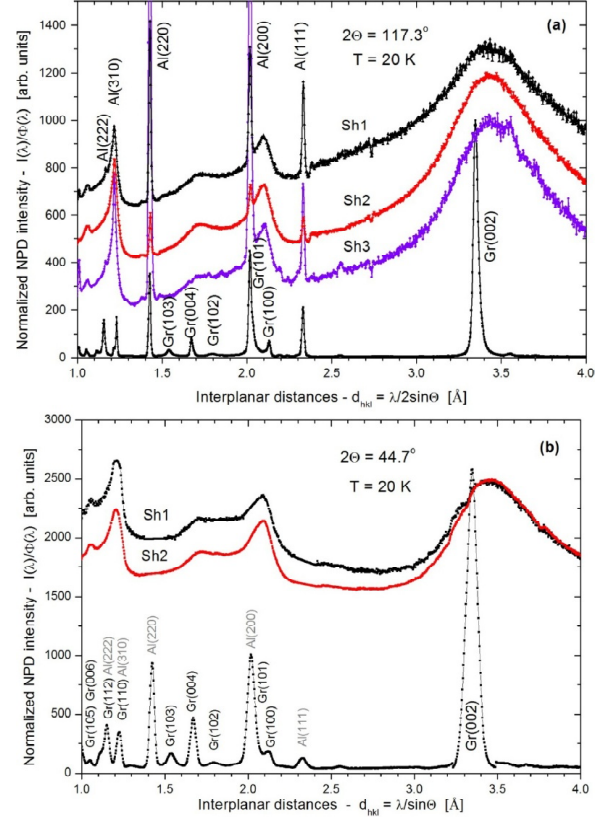


Fig. 6. (a) NPD of spectral graphite (Gr) and shungite carbons Sh1, Sh2, and Sh3 recorded at scattering angle $2\Theta = 117.4^\circ$. (b) NPD of shungite carbons Sh1 and Sh2 after extraction of Al(hkl) reflections. Scattering angle $2\Theta = 44.7^\circ$. The data are normalized per neutron flux intensity at each neutron wave length λ ; Gr(hkl) (black) and Al(hkl) (gray) denote characteristic diffraction peaks of spectral graphite and cryostat (alongside with sample holder) aluminum at different Miller indexes, respectively, data from [2].

$$L_{CSR}^c = (B_{002,ref} / B_{002}) (\lambda / \lambda_{ref}) L_{CSR}^{c,ref}. \quad (7)$$

Substituting λ/λ_{ref} by the ratio of the Gr(002) peak positions $A_{002}/A_{002,ref}$ and using B_{002} values given in Table 2 result in $L_{CSR}^c = 1.3$ nm. Summarizing NPD and X-Ray data [31], L_{CSR}^c of $\sim 1.5 - 2$ nm was sug-

Table 2. Characteristics of Gr(002) peaks of shungite carbons, data from [2].

Samples	Peak position, A_{002} , Å	FWHM, B_{002} , Å
Graphite	3.3501±0.0002	0.0341±0.0006
Sh1		
Sh2	3.4513±0.0015	0.5408±0.0063
Sh3		

gested [1, 2] that corresponds to 5-6 layer structure of the relevant sh-rGO stacks.

As early pointed [32], L_{CSR}^a , which determines the layer lateral dimension, is characterized by the width of Gr(110) peak. On the basis of the Scherrer equation and using results presented in Fig. 6b, the corresponding value can be evaluated following the ratio

$$L_{CSR}^a = L_{CSR}^c \frac{A_{110} \cdot B_{002}}{A_{002} \cdot B_{110}}. \quad (8)$$

B_{110} values of the Gr(110) peak of the three shungite carbons are quite similar and constitute $\sim 0.0723 \text{ \AA}$ so that the relevant $L_{CSR}^a \approx 1.93 L_{CSR}^c$. As known, $\{hk0\}$ reflections are influenced by not only the lateral extent of the graphene layers but the presence of both translational and rotational disorder (turbostratic structure) of the stacks [32]. Therefore, the obtained $L_{CSR}^a \sim 3\text{-}4 \text{ nm}$ can be considered as the upper limit of the lateral size of the sh-rGO sheets while the size of individual sheets might be significantly less.

3.1.2. Ak-GO and Ak-rGO products

Fig. 7 presents a set of the NPD plots, recorded at 20K for the freshly prepared Ak- GO and Ak-rGO samples, alongside with the ones related to spectral graphite - collected at two different angles. The main feature of Ak-GO found in Fig. 7a is described by a broad peak at 7 Å that is equivalent to the Gr(001) reflex forbidden in graphite structure and gives an evidence of a stacked structure with the relevant interlayer distance. The peak is greatly broadened (FWHM constitutes 1 Å) with respect to the reference Gr(002) peak of graphite (FWHM of 0.034Å), which exhibits a considerable size limiting of the stacks normal to the Ak-GO layers. Based on the reported data and following the procedure described in the preceding subsection, it is possible to determine L_{CSR}^c and L_{CSR}^a , the former of which constitutes 1.4 nm and 2.4 nm for the studied Ak-GO and Ak-rGO, respectively, while the latter evidently exceeds 20 nm that marks the low limit of the lateral dimension of layers pointing that it is bigger than the coherent scattering region of crystalline graphite equal to $\sim 20 \text{ nm}$ along a direction [30]. Assuming that the thickness of a GO layer is $\sim 0.6 \text{ nm}$ [9] the Ak-GO stacks may consist of 2-3 layers. Similarly, the thickness of Ak-rGO stacks is about 7-8 layers. The obtained data for both Ak-GO and Ak-rGO samples are in good consistence with the SEM images of the products shown in Fig. 2

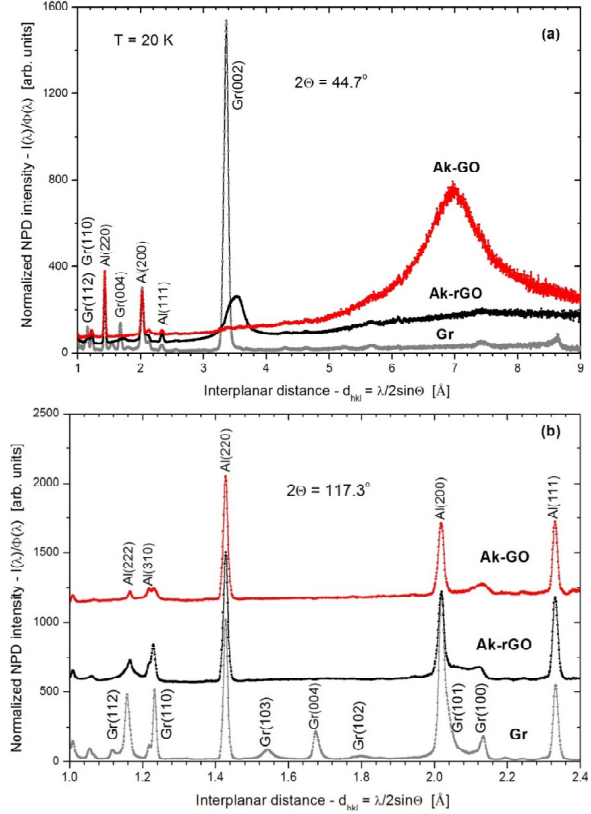


Fig. 7. NPD of spectral graphite (Gr) and Akolab products - graphene oxide (Ak-GO) and reduced graphene oxide (Ak-rGO) - recorded at scattering angles $2\theta = 44.7^\circ$ (a) and $2\theta = 117.4^\circ$ (b) [3]. See details in the caption to Fig. 6.

and other structural studies indicating submicron-micron lateral size of both GO and rGO. The described structures are typical for synthetic GO and rGO of different origin, what has been recently supported by the neutron diffraction study [33].

3.1.3. ppGO and TErGO products

Collected at two different angles, NPD plots in Fig. 8 present data for ppGO and TErGO samples - recorded at 6K- alongside with those related to spectral graphite. The main feature of the ppGO plot in Fig. 8a is described by a broad peak at 7.21 Å, which evidences a stacked structure with the relevant interlayer distance. The peak is noticeably broadened (FWHM constitutes 0.5 Å) with respect to the reference Gr(002) peak of graphite (FWHM of 0.034Å) thus leading to $L_{CSR}^a = 2.9 \text{ nm}$, so that ppGO stacks may consist of 4 layers or more. As for the lateral dimension, data in Fig. 8b show that there are no ppGO peaks broader than the reference graphite ones in the region. It means that the corresponding L_{CSR}^a values of graphite and ppGO are quite

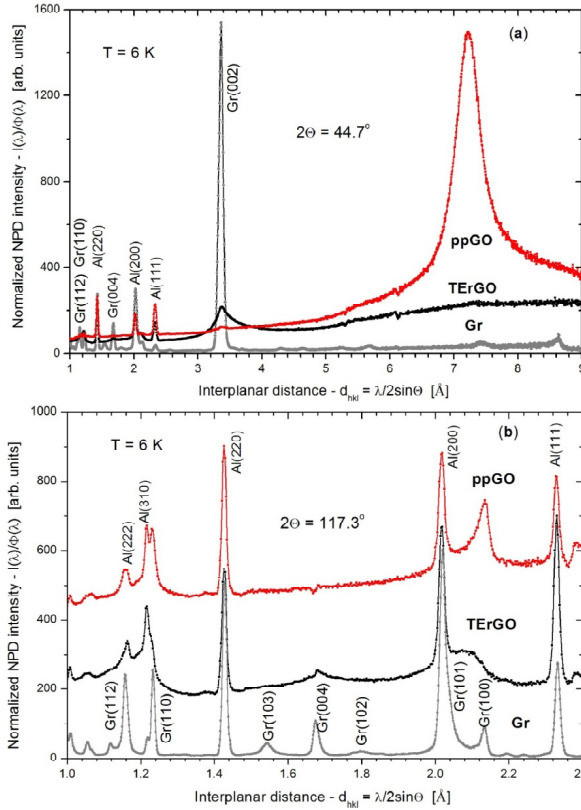


Fig. 8. NPD of spectral graphite (Gr), graphene oxide paper (ppGO) and thermally exfoliated reduced graphene oxide (TErGO) recorded at scattering angles $2\theta = 44.7^\circ$ (a) and $2\theta = 117.4^\circ$ (b), data from [4]. See details in the caption to Fig. 6.

equivalent due to which the lateral dimensions of the GO stacks should be evidently large.

Similar analysis of the Gr(002) peak of TErGO in Fig. 8a (positioned at 3.36 Å with FWHM of 0.26 Å) results in the L_{CSR}^c value of 2.6 nm thus indicating ~8 layer stacks of the TErGO sample. Similarly to the ppGO, none of the diffraction peaks is broadened (see Fig. 8b) in the region below 2.5 Å, which

points to large TErGO stacks in the lateral dimension. The obtained data for both ppGO and TErGO samples are in good consistence with findings of the XRD studies indicating submicron-micron lateral size of both ppGO and TErGO, the SEM images of the products shown in Fig. 3, and recent neutron diffraction study [33].

Table 3 summarizes data obtained for the studied samples. As seen in the table, all the samples present graphite-like stacked structures differing therewith by both the number of layers in the relevant stacks and the lateral dimensions of the layers. As for the latter, all synthetic samples are characterized by large microsize dimension while the natural sh-rGO product is nanoscale. This drastic difference is deeply rooted in the peculiarities of the graphene molecule chemistry, one consequence of which is a consistent fragmentation of the starting molecules up to their nanoscaling in due course of long-term exposure to external reagents [34,35]. Obviously, the geologic scale of time of sh-rGO perfectly suits the condition thus providing its nanoscaling up to the limit size [16].

3.2. Inelastic neutron scattering

3.2.1. INS spectra of shungite carbons

Fig. 9 presents INS TOF spectra of three shungite carbons at $T=20\text{K}$ with the reference spectrum of graphite. As seen in the figure, the scattering intensity from the graphite is so weak that the Gr spectrum practically repeat the background spectrum Al caused by scattering from aluminum accumulated in cryostat and sample holder. The situation does not change remarkably when the graphite mass changes from 10 g to 100 g approaching the mass of Sh1 and Sh2 samples. Therefore, a considerable domination of the scattering from all the three

Table 3. NPD structural data.

Samples	Peak position (Å)	Peak width FWHM (Å)	Number of layers	Layer lateral dimension ¹ (nm)
Graphite	3.35±0.0002	0.034±0.001	~100	>20
sh-rGO	3.45±0.0015	0.548±0.006	5-6	3-4
Ak-rGO	3.50±0.01	0.30±0.01	7	>20
TErGO	3.36±0.01	0.26±0.01	8	>20
Ak-GO	7.00±0.01	1.00±0.01	2-3	>20
ppGO	7.21±0.01	0.50±0.01	4-6	>20

¹The definition >20 nm marks the low limit of the lateral dimension of layers pointing that it is bigger than the coherent scattering region of crystalline graphite equal to ~20 nm along a direction [30]. Actual layer dimensions are of microsize range [3,4].

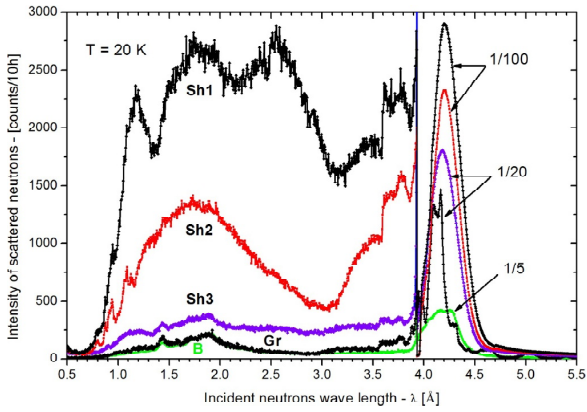


Fig. 9. Time-of-flight INS spectra from shungite carbons Sh1 (1=100 g), Sh2 (2=96 g), Sh3 (3=10 g) and spectral graphite (Gr=10 g). Green curve B presents background from Al cryostat and sample holder material. $T=20\text{K}$. The intensity of elastic peaks is 100-fold, 20-fold, and 5-fold reduced for Sh1 and Sh2, Sh3, graphite and background, respectively. Spectra are summarized over 15 scattering angles and normalized per 10 hours exposition time at constant power of the IBR-2 equal to 1.9 MW.

shungite carbons over the graphite spectrum strongly suggests the hydrogen origin of the shungite INS thus indicating that all of them are hydrogen-enriched. Extracting the Gr spectrum from the shungite ones exempts the latter from the contribution related to the scattering from both aluminum and carbon atoms.

As said in Section 2.1.1, shungite carbons Sh1 and Sh3 should be attributed to *wet* sh-rGO due to containing about 4 wt.% of water under ambient conditions providing the species well developed porous structure [17]. In contrast, shungite carbon Sh2

presents *dry* sh-rGO. Therefore, while spectra Sh1 and Sh3 are evidently provided by a combined effect of retained water and rGO carbon cores spectrum Sh2 presents the carbon core only due to which the difference spectra 1-2 should be attributed to the spectrum of retained water.

Generally, INS TOF spectra are transformed in ω -depending spectra $F(\omega)$ according to Eq. (5) and following one of standard treatment procedures such as described in [26]. However, as shown above, the scattering from heavy atoms can be excluded from the total TOF spectra at the experimental level. Consequently, the transformed ω -spectra, shown in Fig. 10 and related to the TOF spectra in Fig. 9 exempted from the INS spectrum of graphite, present one-phonon AWDVS $G(\omega)$ spectra of hydrogen atoms of the sh-rGO samples. When obtaining $G(\omega)$ spectra, Debye-Waller factors were taken as unity due to low temperature and rather narrow frequency region. The spectra were not corrected on multi-phonon contribution that might be quite noticeable above 800 cm^{-1} even at low temperature [36].

As seen in Fig. 10, $G(\omega)$ spectra of Sh1 and Sh3 are practically identical. Changing in the fine structure of spectrum 3 above 500 cm^{-1} may be connected with either poor statistic of experimental data due to small mass of shungite Sh3 or reconstruction of its structure in the course of transformation of the pristine shungite Sh1 to Sh3 first through dispersion in water and then consolidation of a solid phase after the water evaporation. $G(\omega)$ spectrum of *dry* sh-rGO (Sh2) differs from the above two spectra quite significantly. A detailed discussion of the difference is given in Section 3.3.

3.2.2. INS spectra of Ak-GO and Ak-rGO

The INS TOF spectra of Ak-GO and Ak-rGO versus the incident neutrons wavelength, exempted from the background and carbon atoms scattering are shown in Fig. 11 at low and room temperature. The temperature dependence is typical for molecular solids and is provided by a considerable enhancement of multi-phonon scattering and remarkable smoothing of the total spectrum as a whole [29,36,37]. Both samples scatter the neutrons quite intensely, indicating to be hydrogen-enriched. However, the hydrogen content is quite different in these two cases. Actually, it is quite reasonable to assume that while the hydrogen atoms in retained water play the main role in the hydrophilic Ak-GO - whose spectrum is definitely alike to that of wet GrO [38], the ones incorporated in the carbon core

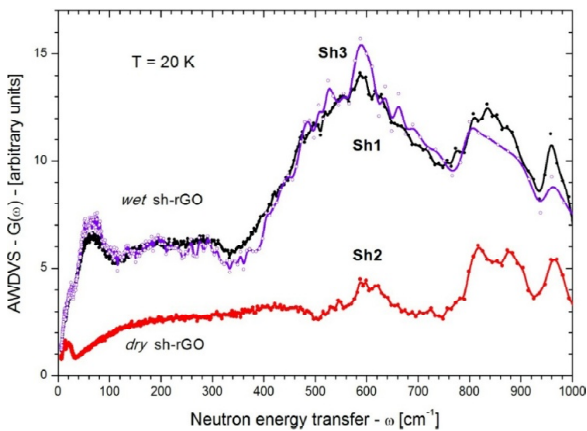


Fig. 10. Experimental one-phonon amplitude-weighted density of vibrational states (AWDVS) $G(\omega)$ spectra of *wet* (1-Sh1 and 3-Sh3) and *dry* (2-Sh2) shungite carbons normalized per 10 g of mass.

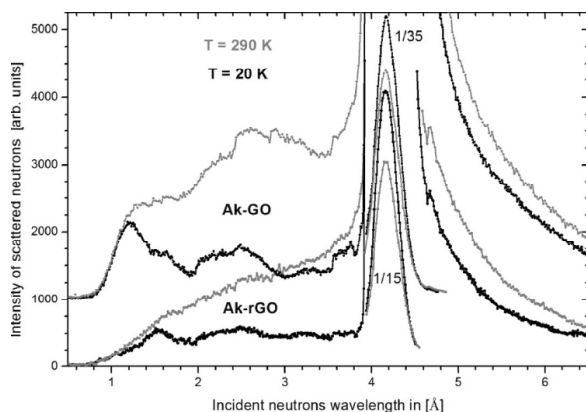


Fig. 11. Time-of-flight INS spectra of Ak-GO and Ak-rGO, recorded at $T=20\text{K}$ (black) and 295K (light gray), normalized by monitor counter to the same number of incident thermal neutrons flux for the wavelength region ($0.8 - 6.8$) Å, and exempted of background and scattering spectrum of graphite, data from our work [3]. The intensity of elastic peaks of Ak-GO and Ak-rGO spectra is 35- and 15-fold reduced, respectively.

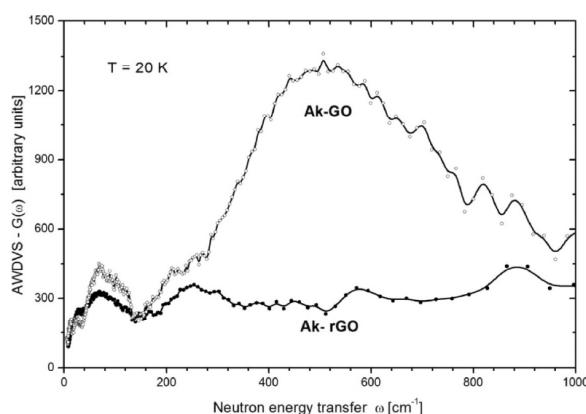


Fig. 12. Experimental one-phonon amplitude-weighted density of vibrational states (AWDVS) $G(\omega)$ spectra of Ak-GO and Ak-rGO at 20K , data from our work [3]. The spectra are normalized per 10 g of mass.

of hydrophobic Ak-rGO take the responsibility in the second case.

Similarly to the case above, the TOF spectra in Fig. 11 are transformed into one-phonon AWDVS $G(\omega)$ spectra, low-temperature GO and rGO components of which are presented in Fig. 12 and discussed in Sections 3.3.1 and 3.3.2, respectively.

3.2.3. INS spectra of ppGO and TErGO

Fig. 13 presents the similarly obtained low-temperature $G(\omega)$ spectra of ppGO and TErGO. As seen in the figure, ppGO sample scatters quite intensely thus indicating to be evidently hydrogen-enriched

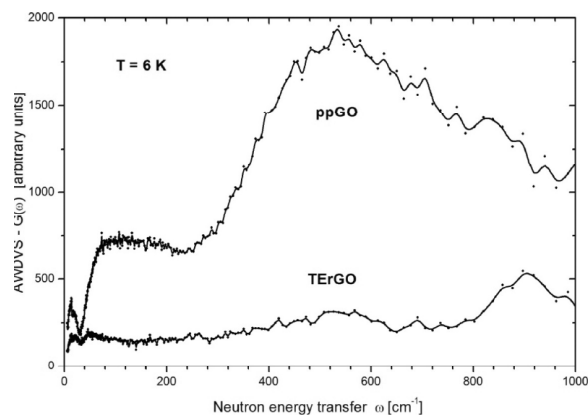


Fig. 13. Experimental AWDVS $G(\omega)$ spectra of ppGO and TErGO at 6K , data from our work [4]. The spectra are normalized per 10 g of mass.

while scattering from TErGO sample is much weaker. As follows from Fig. 4a, freshly prepared ppGO contains a significant amount of retained water that is obviously responsible for the sample INS. On contrast, the quantity of the retained water in the freshly made TErGO is much smaller (see Fig. 4b). The TErGO spectrum quite differs from that of retained water due to which it should be mainly attributed to hydrogen atoms incorporated in the carbon skeleton of the hydrophobic TErGO similarly to chemically produced Ak-rGO [3] and natural *dry* sh-rGO [1,2].

3.3. Comparative analysis of the experimental spectra

3.3.1. Retained water spectra

As shown in the preceding sections, INS spectra of the three kinds of the studied samples form two distinct groups. The first combines GO partners of synthetic families and *wet* sh-rGO while the second covers spectra of *dry* sh-rGO and other two synthetic rGOs. Spectra of the first group are given in Fig. 14. Since the relevant GO matrices of Ak-GO and ppGO are not hydrogen rich and consist of carbon and oxygen atoms [9], the dominant parts of their $G(\omega)$ spectra should be attributed to the retained water, due to which $G(\omega)$ spectra presented in Figs. 14c and d exhibit the latter. Similarly, shungite carbon is also presented in Fig. 14b by the spectrum of retained water (sh-water) that is the difference of spectra of *wet*(1) and *dry*(2) shungite carbons shown in Fig. 11. Additionally, the NERA spectrum of I_h ice is given in Fig. 14a for comparison.

As seen in the figure, evidently, the water spectra of the studied sample have much in common: all

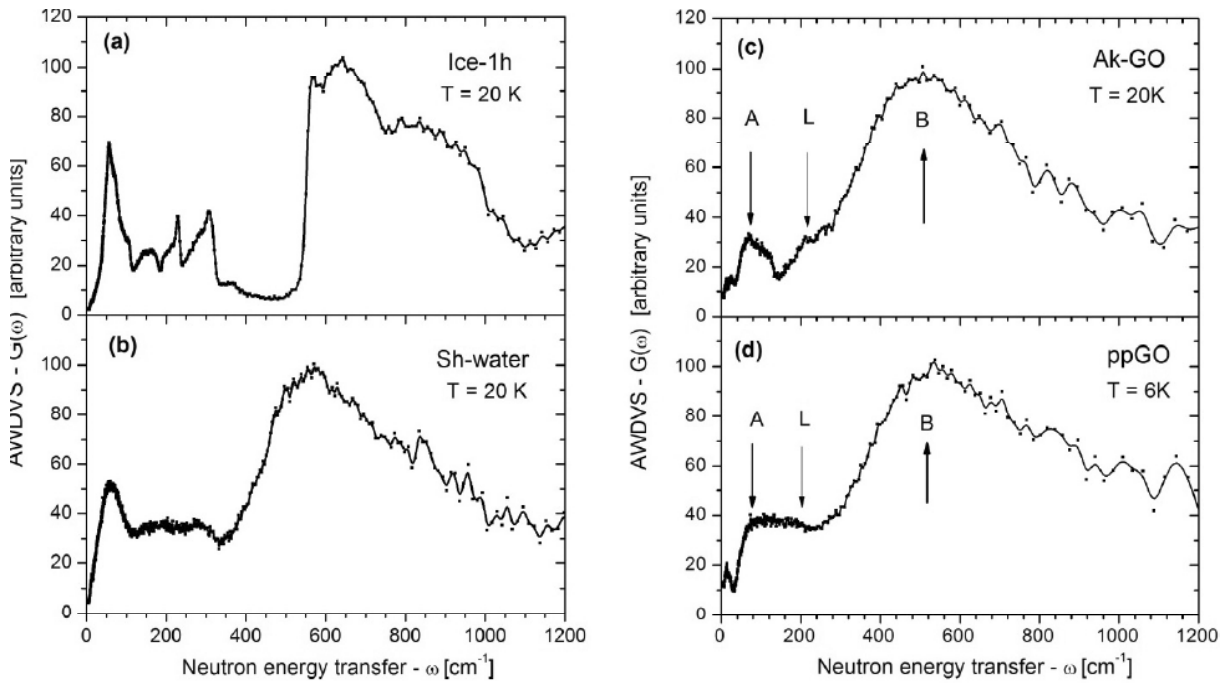


Fig. 14. Experimental AWDVS $G(\omega)$ spectra of of I_h ice (a), retained water in shungite carbon (b); Ak-GO (c); and ppGO (d).

of them involve three parts characteristic for the bulk water, namely: dominant in intensity B band in the region of 500-600 cm^{-1} , less intense A and L bands in the regions of $\sim 100 \text{ cm}^{-1}$ and 200-300 cm^{-1} . These peculiarities are doubtless reflections of similar features of the bulk water (ice) spectrum and can be attributed to rotational (libration) modes (B) and hindered translational mode (A and L). As well known [39], both the hindered translational and rotational modes are present in bulk water because of intermolecular hydrogen bonds (HB) that are formed by each water molecule surrounded by other four ones. Evidently, the configuration changes when water molecules cannot freely move because of confining geometry due to which it is quite natural to expect a visible modification of water spectrum when passing from the bulk to retained water. As seen in Fig. 14, actually, spectra of retained water differ remarkably with respect to the ice spectrum. However, the less change is characteristic for sh-water spectrum while in the case of the Ak-GO and ppGO spectra of GO samples, the changes are so considerable that one can speak about a drastic changing of water molecule behavior; therewith, both latter spectra are quite similar. The observed peculiarities are resulted from the confining geometries where water is retained.

INS study of retained water has a long history in the course of which among other important issues, a considerable attention was given to the topology of confining geometries [40-44]. According to sug-

gested classification, the sh-water spectrum should be attributed to the spectrum of water retained in pores while Ak-GO and ppGO spectra are characteristic for interlayer confining. This conclusion is well consistent with our presentation of the sample structure. Actually, detailed adsorption [45] and small-angle neutron scattering (SANS) [46] studies evidenced a peculiar porous structure of shungite carbon with two sets of pores of $<10 \text{ nm}$ and of $\sim 100 \text{ nm}$ lateral dimensions formed by stacks (of 4-7 layers according to Section 3.1) of hydrophobic nanosize rGO sheets [16]. On the other hand, laterally extended a few layer stacks of hydrophilic GO willingly retain water between the layers similarly to GrO [36].

Fig. 15 presents a general view on $G(\omega)$ spectrum of water retained in a porous matrix [40,42,47,48]. As seen in the figure, the spectrum does not practically depend on the hydration degree due to which two cases related to fully filled pores and wetted over the surface region only are not remarkably different. This means that the water interaction with the inner surface of the pores is weak so that the molecules both near the surface and in the pore depth move quite freely. The latter is supported by the spectrum shape that deviates from the spectrum of bulk water (see Fig. 14b) rather little. Nevertheless, the deviations are clearly fixed. They concern flattening and downshift of bulk hydrogen bond (HB) bendings at $\sim 150 \text{ cm}^{-1}$ and HB stretchings at ~ 224 and $\sim 296 \text{ cm}^{-1}$. A certain modi-

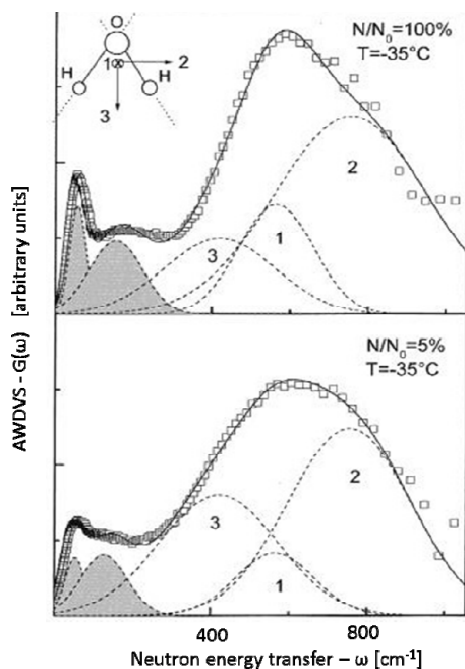


Fig. 15. Experimental AWDVS $G(\omega)$ spectra of water confined in Gelsil porous glass at relative humidities N/N_0 of 100% and 5% together with the deconvoluted Gaussian components, corresponding to two translational modes (filled area) and three librational ones (dashed curves) around three symmetry axes of water molecules. The inset shows three possible symmetry axes: axis 1 perpendicular to the molecular plane, axis 2 in the molecular plane, and axis 3 the 2-fold molecular symmetry axis, adapted from [40].

fication of bulk spectrum takes place in the region of librational modes forming a broad band in the region of 600-1200 cm^{-1} . As shown in Fig. 15, the band is provided with water molecule rotations around three symmetry axes whose partial contribution determines the band shape. The modes conserve their dominant role in the spectra of retained water, albeit are downshifted, and downshifted rather differently when water molecules are either coupled with the pore inner surface or with each other. A comparison of Fig. 14b and Fig. 15 evidently shows that the very behavior is characteristic for the sh-water spectrum. Obviously, the spectrum three-ax partial contribution is sensitive to both chemical composition of the pore walls and the pore size [40]. Thus, the downshift of the red edge of band B from 550 cm^{-1} to 320 cm^{-1} when going from the bulk water to retained water in shungite carbon highlights the shungite pore size of a few nm, which is well consistent with the adsorption and SANS data [45,46].

In contrast to sh-water, Ak-GO and ppGO spectra in Figs. 14c and 14d clearly reveal features characteristic for the water retained in the interlayer space of GrO [38]. As shown, the bulk water spectrum considerably deviates in the region of translational modes (covering both HB bending (A) and stretchings (L)) while the intense librational band B is broadened and downshifted similarly to B band in the sh-water spectrum. Evidently, the observed deviations are caused by different factors, among which but a few there are the explicit chemical composition of the GO basal planes, the number of GO layers in stacks, the shape of the relevant GO sheets, the lateral size of the sheets, and other. The influence of some of these factors will be discussed in Section 4.2. Due to high variability of GO materials over all these parameters [10-14,20], one should expect a remarkable variety of their INS spectra that is observed in the two studied cases.

3.3.2. rGO spectra

Analyzing INS spectra of rGO samples, one should conclude that a considerable intensity of the INS is caused by hydrogenation of their carbon skeletons. The fixation of the interlayer distance in the rGO stacks in all the studied cases within 3.4-3.6 Å evidences that the relevant hydrogen atoms occupy the circumference (*ccf*) area of the rGO sheets due to which the latter should be attributed to framed *ccf* oxyhydrides of graphene (FOHG). Similarly to GOs, FOHGs are highly variable by chemical composition, size, and shape [10-14,20] and their properties are largely varied. The latter should be naturally attributed to the INS spectra as well. However, since the hydrogen contribution mainly provides the INS spectra recording one should expect a certain similarity in the spectra behavior. This turns out to be a real fact, which is illustrated in Fig. 16.

Curves in left (a-c) panels of Fig. 16 present $G(\omega)$ spectra of the studied samples recorded at the NERA spectrometer at IBR-2 at JINR (NERA spectra below). The spectra evidently demonstrate a general similarity of the rGO bodies while their difference in details can be considered as a convincing proof of the matter variability. Do not satisfying by these general statements, let us try to scrutinize the issue in more details. The obtained spectra are provided by the motion of two groups of atoms, namely: hydrogens located in the *ccf* area and carbons of the graphene-like cores. Vibrational frequencies follow this division and allow attributing the spectral range below 800 cm^{-1} to graphite-like

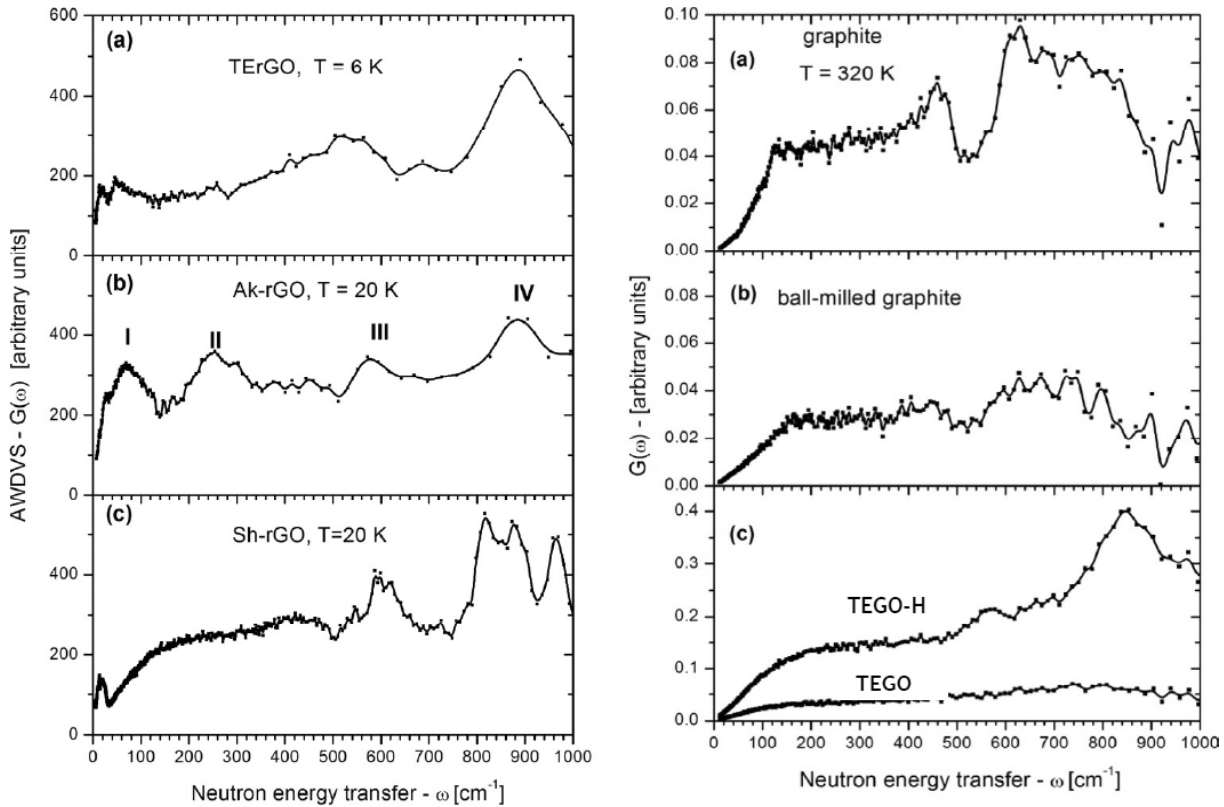


Fig. 16. Experimental AWDVS $G(\omega)$ spectra. Left – NERA spectra: (a) TErGO [4]; (b) Ak-rGO [3]; and (c) sh-rGO [1,2]. Right – ILL spectra: (a) graphite; (b) bill-milled graphite; (c) thermally exfoliated nanosize rGO (TEGO) and hydrogenated TEGO (H-TEGO) recorded at the IN1 spectrometer at the HFR in the ILL, adapted from [49].

modes mainly while above the region – to vibrations of C-H bonds [3,22]. The fact that the low-frequency vibrational modes are well pronounced in the discussed spectra is connected with ‘riding effect’ caused by the contribution of hydrogen atoms displacements in the wave vectors of the carbon atoms modes (see detailed discussion of the effect in Section 2.3). In view of this, the difference in the (a)-(c) spectra below 800 cm^{-1} may result from two facts related to changes either in chemical composition of the *ccff* framing of the studied FOH or in the graphite-like vibrational modes of the relevant carbon cores. Such a vision of the situation has recently obtained a serious support based on the study of a set of graphite-like and graphene-like samples at the thermal neutron source of the ILL [49].

Thanks to kind permission of the authors (S.R. and C.C.), $G(\omega)$ spectra in right (a-c) panels of Fig. 16 reproduce data obtained in the ILL (ILL’s spectra below). The study was concentrated on disclosing the coherent INS from carbon atoms thus obtaining parent (a), bill-milled (b) graphite and nanosize graphene TEGO (c) scattering. The latter sample presents rGO obtained in due course of the thermal exfoliation of GrO (produced from the parent graph-

ite as well) in the inert atmosphere. Taking together, the ILL carbon data exhibit changes in the $G(\omega)$ spectra when passing from macroscopic graphite to mesoscopic bill-milled graphite and nanoscopic TEGO, thus disclosing changes in the behavior of graphite-like phonon modes due to decreasing size parameters. Evidently, while $G(\omega)$ spectrum of graphite (a) well reproduces all the features of the calculated density of states (DOS) of graphite [50] the reduced dimensions of the grains in bill-milled graphite (b) and TEGO (c) have strong effects on the dynamic properties: peaks in the density of states progressively broaden, with an increased proportion in the low frequency part of the spectrum [49].

Comparing the discussed ILL $G(\omega)$ spectra with the NERA ones presented on the left panels of Fig. 16, it is easy to note that the size reducing is clearly come out in the latter when passing from TErGO to sh-rGO within the family. Comparing the spectra of the two sets, it is clearly seen that the TErGO left spectrum is well similar to the right spectrum of the parent graphite while the right TEGO and TEGO-H spectra are well similar to the sh-rGO one. These findings are well consistent with microsize lateral dimension of both TErGO and graphite samples

while nanosize dimensions of sh-rGO as well as TEGO and TEGO-H suit each other quite perfectly thus making it a convincing evidence of a decisive role of rGO sheets size for the appearance of the DOS of their vibrational states. As for the Ak-rGO spectrum, its deviation from the TErGO and sh-rGO ones definitely evidences changing dimensions of the sample from the two above. However, the changing is much more significant than caused by ball-milling while revealing therewith a particular reconstruction in the DOS spectrum of the carbon vibrational states.

Considering both the NERA and ILL spectra until now, we have mainly been concentrated on the spectral range below 800 cm^{-1} . However, all the NERA spectra as well as the ILL H-TEGO spectrum (right (c) panel) show well pronounced features above the region, quite similar in all the spectra. As shown in [3,28], the region is characteristic for non-planar deformational vibrations of C-H units that mainly contribute into framing of FOHG under the presence of hydrogen. The observed transformation of the ILL TEGO and H-TEGO spectra, caused by the TEGO additional hydrogenation, supports this conclusion directly. We shall come back to the point in Section 4.3.

4. A COMPARISON OF EXPERIMENTAL $G(\omega)$ SPECTRA WITH CALCULATED DATA

4.1. Computational models used

4.1.1. {GO + water} model

Obviously, the successful outcome of a comparative analysis of experimental and calculated $G(\omega)$ spectra depends on two circumstances: 1) how well the atomic-structural models, underlying the calculations, suits the real structure of the studied samples; and 2) how accurate is the vibrational problem solution. Below we shall consider the first issue while the second one is satisfactorily ensured when precisely optimized equilibrium geometries of model structures are subjected to the vibrational analysis by using the finite displacement method [3,4,28].

According to experimental evidences, the model, suitable for describing the INS from GOs, should involve a stack of GO layers, each of which is covered by a monolayer of water molecules bound to the GO core via HBs. Therefore, a proper {GO+water} model should involve two components, namely, individual GO layers separated by 7 \AA in average and a set of water molecules, forming monolayers around

the former. The choice of a specific GO model is the main problem. The matter is that, as said before, the term 'GO' covers a very large class of complex polyderivatives of graphene sheets, once graphene molecules, differing by many factors, among which there are: 1) the size and shape of parent graphene molecules that are the carbon cores of the derivatives; 2) the total number of addends involved in the species formation; 3) the addend distribution over the basal plane and circumference of the graphene molecule; 4) the addend chemical variety; 5) finally, the extent of the oxygenation of the molecules, and so forth. Following the legal language, this fact makes a simple term GO to the term with 'the encumbrance'. This 'encumbrance' is also the reason of a wide range of the GO structural models reported, while none of them can satisfy the entire set of experimental data [12,13]. The latter might be partially due to the fact that separate portions of the data are obtained in different labs on possibly different products. It is better to said, that in the case of the GO model, we can speak not about a unique standard model, but about its averaged representation. Moreover, when designing this averaged model, one should take into account the physical method of testing by which it will be justified, since all the methods are differently sensitive to both the GO structural features and its chemical composition. Thus, in the case of INS experiments, a particular attention should be given to the hydrogen atoms involved in the model.

The model - suggested in [28] and presented in Fig. 17a – suits the case and can be considered as such an averaged one. The size of the GO molecule is determined by the parent (5,5) graphene sheet (the latter is presented by a rectangular graphene fragment containing $n_a=5$ and $n_z=5$ benzenoid units along the armchair and zigzag edges, respectively). As has been shown, the molecule of this size is large enough to reliably reveal the main peculiarities of the molecular chemistry of graphene [6,9,51]. It is widely accepted by now that the atomic oxygens and hydroxyls (mainly) as well as carboxyls (in minority) take part in the graphene oxygenation, resulting in the formation of epoxy and hydroxy groups on the molecule basal planes, while the carbonyls, hydroxyls, and carboxyls are spread over the circumferences (see a detailed analysis in [9]). The distribution of these OCGs over the carbon core is not standard and may widely vary, depending on the chemical protocol in use as well as on external conditions of the oxygenation. However, atomic content related to real products may give some insight into the averaged distribution.

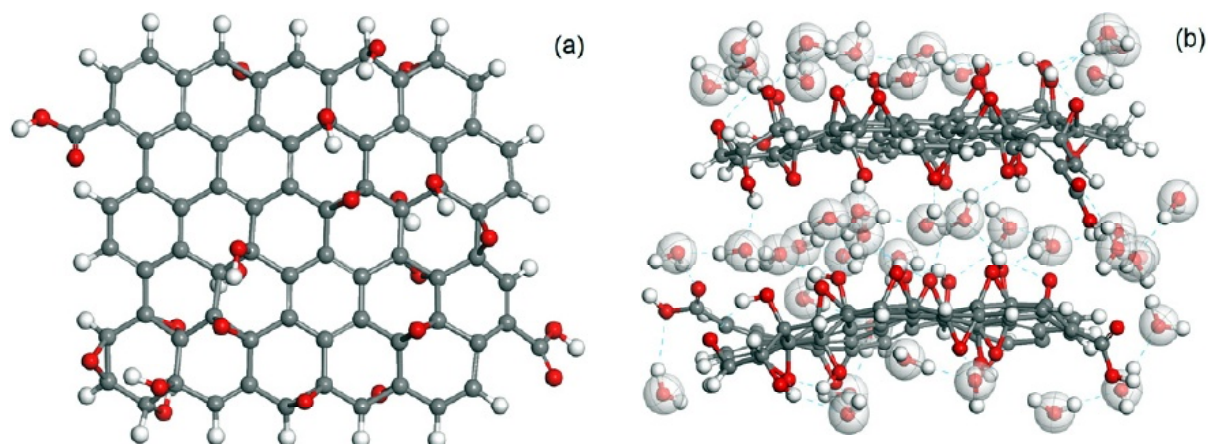


Fig. 17. Equilibrium structure of the {GO+water} model. (a). (5,5) GO molecule. (b). Two-layer solvated sandwich of (5,5) GO molecules including 48 water molecules (see detail description in [3]). Gray, red and white balls present carbon, oxygen, and hydrogen atoms, respectively.

As shown in Table 1, the atomic mass content of the studied GO products can be approximately presented by per-one-benzenoid-ring chemical formula $C_6O_3H_2$ for Ak-GO [3] and $C_6O_3H_{0.85}$ for ppGO [4]. The (5,5) GO molecule presented in Fig. 17a involves both epoxy ($\times 11$) and hydroxy ($\times 8$) groups that are randomly spread over both sides of the basal plane (containing 44 carbon atoms), which corresponds to the average formula $C_6O_{2.5}H_{1.2}$ that is close to the above ones. Since, as shown earlier, the contributions of C^{12} and O^{16} isotopes into INS are practically negligible, the contribution of the basal-plane atoms in the experimental spectrum is mainly provided due to the incoherent scattering from hydrogen atoms of hydroxyls.

In addition to carbon atoms forming the basal plane, the chemical composition of the GO circumference is of great importance. Usually, this area is presented by carbonyls, hydroxyls, and carboxyls, among which only two latter contribute to INS. To make the circumference contribution more vivid, the edge atoms are intentionally terminated with hydrogens. Such a termination gives a possibility to trace the changes of the INS spectra of GOs in the course of their transformation to rGOs, since the appearance of hydrogen atoms in the GO circumference is a direct evidence of the reduction (see detailed discussion in [2]).

Fig. 17b shows the double-layer ‘solvated sandwich’ of two (5,5) GO molecules surrounded by 48 water molecules. The mass contribution from water was estimated as $\sim 36\%$, which exceeds that expected from mass-content experimental data. However, the excess of the molecules allows understanding the peculiarities in the INS spectrum of water in more details. A detailed analysis [3] shows that none

of the molecules is dissociated and each of them form the HBs with GO layer (either $H-O=$ with epoxy groups or $O-HO$ with hydroxyls) that are supplemented with one-two HBs with neighboring water molecules.

4.1.2. rGO models

rGO models are tightly connected with those of pristine GO ones thus relating to the latter when removing all OCGs from the sheet basal plane. A large variety of GO models are mainly just pencil-made basing on a chemical intuition. On this background, there is a definite preference of that one produced in due course of a sequential polyderivatization of a graphene flake [9] in the framework of the computational experiment subordinated to a particular algorithm. Thus constructed (5,5) GO molecule is shown in Fig. 18a. The latter was computationally synthesized in the course of the stepwise oxidation of the pristine (5,5) graphene molecule in the presence of three oxidants, such as O, OH, and COOH [9]. The GO reduction concerns removing oxygen containing units. As evidences by the *per step* coupling energies, which accompany the attachment and/or removing of the oxidants to either basal plane atoms (curves 1 and 2 in Fig. 18b) or edge atoms in the circumference area (curve 3), the reduction is obviously multistage or multimode one. Actually, the oxygen atoms located at the basal plane of the pristine (5,5) GO molecule (within the rose shading) should be removed first. The corresponding (5,5) rGO molecule is shown in Fig. 18c. This apparently happens at the first stage of the real reduction and may present the final state of the reduction procedure when the latter is either short-time or not very effi-

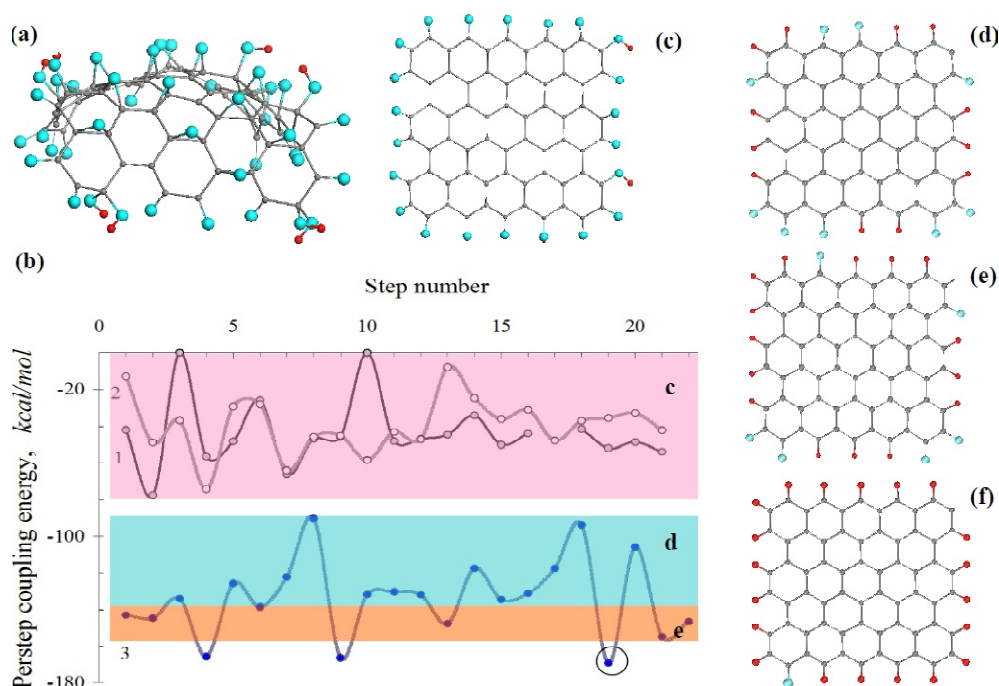


Fig. 18. (a). Equilibrium structure of ~ 1 nm (5,5) GO sheet corresponding to one-side oxidation of the pristine (5,5) graphene molecule [9]. (b). *per step* coupling energies related to the one-side oxygenation of the (5,5) graphene molecule: O- and OH-attachments to the basal plane (curves 1 and 2, respectively) and the combination of O and OH attachments in the circumference (curve 3) [9]; the circled point corresponds to the formation of carbonyl unit on the rGO circumference with the largest coupling energy. (c). Model (5,5) rGO sheet corresponding to the first stage of the (5,5) GO deoxygenation that affects the atoms in the basal plane of the GO sheet only (c area in (b)) (soft reduction) [2]. (d) and (e) Model (5,5) rGO sheets corresponding to a medium and hard reduction of the (5,5) GO in the framework of the blue (d) and cream (e) shaded zones in (b), respectively. (f) Model (5,5) rGO sheet corresponding to circled point in (b). Gray, blue and red balls present carbon, oxygen, and hydrogen atoms.

Table 4. Chemical composition and mass content of differently reduced (5,5) rGOs.

Atomic composition	Mass content, wt.%			Remarks
	C	O	H	
$C_{66}O_{22}H_2$	69.13	30.70	0.17	calc., Fig. 18c
$C_{66}O_9H_{13}$	83.46	15.17	1.37	calc., Fig. 18d
$C_{66}O_6H_{16}^*(C_6O_{0.54}H_{1.45})^{**}$	87.6	10.6	1.8	calc. Fig. 18e
TErGO	87.1 ± 0.3	12.1 ± 0.3	0.5 ± 0.3	Exp. [4]
$C_{66}O_3H_{19}^*(C_6O_{0.27}H_{1.73})^{**}$	92.2	5.6	2.2	calc. Fig. 20
Ak-GO	92.0 ± 1.0	5.5 ± 0.5	1.5 ± 0.5	Exp. [22]
$C_{66}O_1H_{21}^*(C_6O_{0.09}H_{1.91})^{**}$	95.5	1.9	2.5	calc. Fig. 18f
sh-rGO	$95.3-92.4^{***}$	$3.3-2.5^{***}$	$2.0-0.7^{****}$	Exp. [20]
$C_{66}H_{22}$	97.30	-	2.70	calc.

* Proposed (5,5) rGO compositions that best fit experimental data.

** Averaged mass content per one benzenoid unit.

*** The scatter in the data obtained from measurements in four points of one sample [20].

**** The hydrogen content is difficult to determine due to which only the range is definitely fixed [20].

cient; the relevant reduction might be attributed to a soft one. The corresponding mass content of the obtained rGO molecule is given in Table 4.

However, when the reduction occurs during long time or under action of strong reducing agents, it may concern oxidants located at the rGO molecules

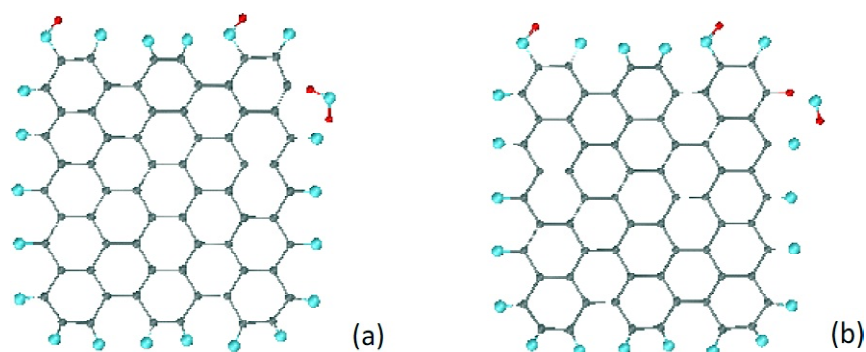


Fig. 19. a. Starting configuration of the complex of one water molecule and the soft-reduced (5,5) rGO molecule after removing one oxygen atom in the circumference. (b). Equilibrium structure of the (5,5) rGO + water complex (UHF calculations). The atom colorings see in the caption to Fig. 18.

circumference. Such two-step reduction of a pristine GO has been actually fixed [52]. However, due to a waving character of the *per step* coupling energy dependence with a large amplitude from -90 kcal/mol to -170 kcal/mol, the second step reduction could be highly variable. Thus, limiting the energy interval to 30 kcal/mol (removing oxidants covered by blue shading) results in remaining only 9 oxygen atoms (see Fig. 18d) instead of 22 in the pristine (5,5) rGO sheet shown in Fig. 18c. As seen in Table 4, such a reduction halves the oxygen content and causes the appearance of a remarkable quantity of hydrogen. Further strengthening of the reduction, counted by lowering the number of remaining oxygen atoms, gradually decreases the oxygen content while increasing the hydrogen contribution. Consequently, the structures shown in Figs. 18c, 18e, and 18f might be attributed to rGOs obtained in the course of soft, medium, and hard reduction, respectively, thus presenting a large series of different FOHGs.

Coming back to the rGO succeeding hydrogenation, we face the problem, whence comes the hydrogen. Neither synthetic, nor natural GO are rich of hydrogen due to which GO sheets similar to that shown in Fig. 18a do not contain hydrogen among its framing atoms. However, the release of one of the edge carbon atoms of the rGO within the blue zone shown in Fig. 18b from oxygen makes the atom highly chemically active [51] and promotes the dissociation of a water molecule in the vicinity of this atom and neighboring oxygen. A possibility of such reaction is demonstrated in Fig. 19. The water molecule, initially located at 1.10 Å apart from both the carbon and oxygen atoms in Fig. 19a, willingly dissociates (see Fig. 19b) while the formed hydroxyl remains in the vicinity of the newly formed C-H bond, once connected with both the bond hydrogen atom and neighboring oxygen via hydrogen

bonds. The energy gain of the reaction constitutes 25.94 kcal/mol which points to a high efficacy of the reaction. Evidently, the considered mechanism of the rGO hydrogenation, parallel or alongside with the simultaneous GO reduction, might not be the only one and will strongly depend on the reducing agents such as, for example, alcohols under critical regime [22,24]. Actually, hydrophobic character of produced rGOs, oppositely to high hydrophilicity of the pristine GO, which is noted by many chemists, strongly evidences the reality of the hydrogenation of initially produced rGOs.

When supposing that in due course of the hydrogenation of the rGO molecule each of the remaining oxygen atoms is substituted by one hydrogen, the limiting case, presented by C₆₆H₂₂ framed polyhydride in Table 4, corresponds to the one-atom-hydrogen termination of the edge atoms of the (5,5) graphene sheet. However, as shown in [53], in this case, the edge atoms remain yet still chemically active and are able to accept one more hydrogen atom each. The addition of the second hydrogen atom in response to removing one oxygen atom can occur at any stage of the hydrogenation of the circumference area. However, this action influences the oxygen content only slightly due to which the data presented in Table 4 may be used for estimation of the C/O ratio. In contrast, the hydrogen content may considerably increase thus greatly lifting the INS intensity, which should be taken into account when analyzing INS spectra.

As seen in Table 4, model rGO molecules C₆₆O₆H₁₆ and C₆₆O₁H₂₁, presented in Figs. 18e and 18f, fit the mass content of the NERA TErGO and sh-rGO products and can be considered as suitable models for the case. The third C₆₆O₃H₁₉ molecule suitable for modelling Ak-rGO is shown in Fig. 20. However, due to undeniable domination of hydrogen atoms in INS scattering, the three models

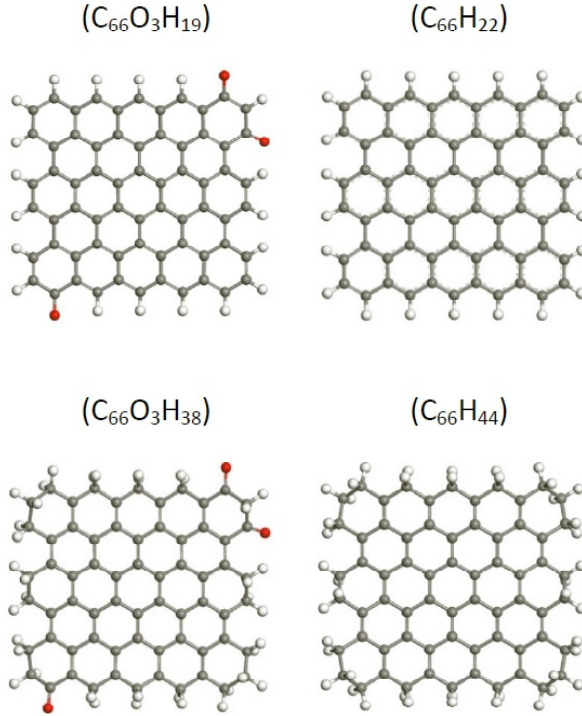


Fig. 20. Equilibrium structures of (5,5) rGO molecules presented by $C_{66}O_3H_{19}$ and $C_{66}O_3H_{38}$ oxyhydrides (left panels) as well as by $C_{66}H_{22}$ and $C_{66}H_{44}$ hydrides (CH1 and CH2 models, respectively) (right panels). Atom marking see in the caption to Fig. 17.

can be reliably substituted by either $C_{66}H_{22}$ or $C_{66}H_{44}$ (see Fig. 20), which provides a full opportunity to investigate the behavior of any rGO under interaction with neutrons.

4.1.3. About ‘riding effect’ again

The models under discussion, namely, {GO+water} as well $C_{66}H_{22}$ and/or $C_{66}H_{44}$, consist of H^1 , C^{12} , and O^{16} isotopes. The peculiarities of the INS caused by such nuclear content, was discussed in Section 2.3. Fig. 21 presents data for the former model in the same manner as it was done in the case of $C_{66}H_{22}$ molecule (see Fig. 5). Two pairs of $\sum_n |A_j^n(\omega)|^2$ and $F(\omega)$ data are exhibited with respect to the total {GO+water} model and its part related to the (5,5) GO molecule. The $|A_j^n(\omega)|^2$ data in the bottom panels of both pairs are summarized over carbon (gray), oxygen (red) and hydrogen (blue) atoms for each vibrational j -mode provided that $\sum_n |A_j^n(\omega)|^2 = 1$ (100%). Black bars and their convolutions by using Lorentzians of 80 cm^{-1} half width (black curves) of the $F(\omega)$ panels present the cumulated contribution of all the isotopes in ω -dependent INS scattering intensity according to Eqs. (1) and (5).

As seen in the figure, vibrational modes of GO at the bottom panel of the figure in the chosen frequency interval are mainly provided by oxygen and carbon atoms while the contribution of hydrogen atoms into each of the modes does not exceed a few percents. At the same time, $F(\omega)$ curve repeats the shape of the $|A_j^n(\omega)|^2$ distribution over hydrogen atoms thus demonstrating a strong ‘riding effect’ and allowing substituting $F(\omega)$ function by $G(\omega)$ quite accurately. The inaccuracy of this substitution does not exceed 10% due to which in what follows we shall refer to $G(\omega)$ spectra only. When the hydrogen atom contribution into vibrational modes increases, as it is in the case of the {GO+water} model at the top panel of the figure, the inaccuracy evidently becomes less and attribution of the $F(\omega)$ to $G(\omega)$ is more valid.

4.2. Calculated INS spectra of the GO core and retained water

The calculated $G(\omega)$ spectrum of the {GO+water} model, suitably partitioned over different contributions, is shown in Fig. 22. The spectrum of the (5,5) GO molecule (Fig. 22a) is provided with two constituents related to CH and OH units. It should be noted that not only vibrations of the units themselves but carbon and oxygen atoms via the ‘riding effect’ discussed above contribute into the molecule $G(\omega)$

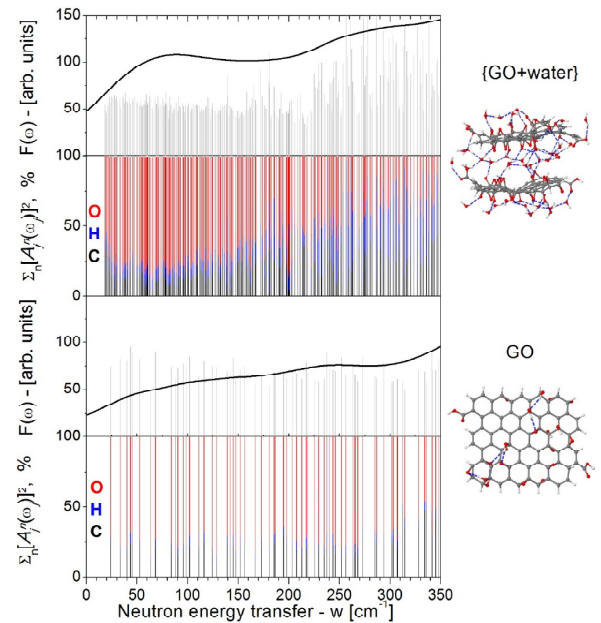


Fig. 21. Quantitative evaluation of the accuracy of the AWDVS approximation and ‘riding effect’ related to graphite-like vibrational modes. Dark, red and blue bars mark the contribution of carbon, oxygen, and hydrogen atoms, respectively (see text).

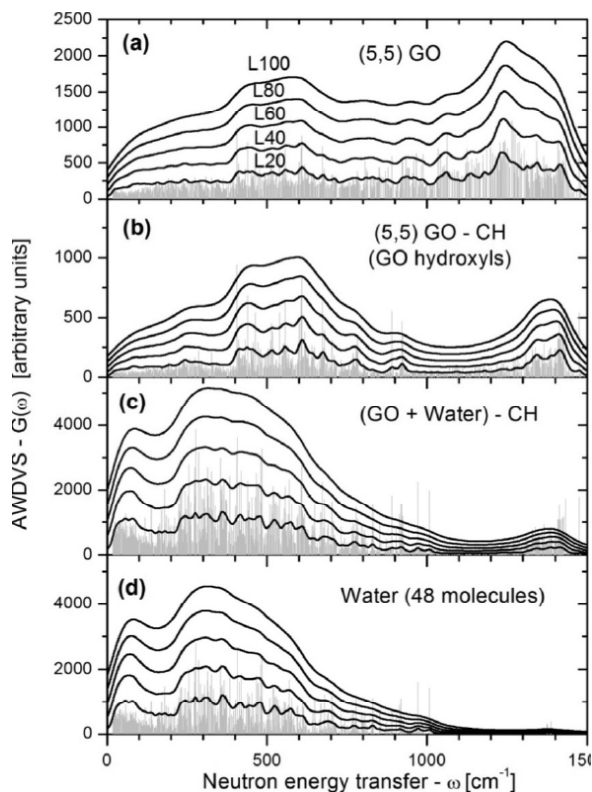


Fig. 22. AWDVS $G(\omega)$ spectra of the $\{\text{GO}+\text{water}\}$ model (see Fig. 17) calculated at the rPBE/DNP level of theory [28]. (a). Total spectrum of two (5,5) GO molecules (see Fig. 17a), (b). Total spectrum of two (5,5) GO molecules exempted from the contribution caused by CH units. (c). The same as in (b) but for $\{\text{GO}+\text{water}\}$ model. (d) The spectrum of involved 48 water molecules. The 0-1 INS vibrational mode intensities (light gray bars) were convoluted by using Lorentzians of 20, 40, 60, 80, and 100 cm^{-1} half width (black lines L20, L40, L60, L80, and L100, respectively). The labeling is attributed to all panels. At each panel all the spectra are given in the same scale. Y axes in panels (a) and (b) are 2.4-fold and 4-fold scaled, respectively, to make the relevant contributions into the total spectrum of the model more pronounced.

spectrum. The riding effect is mainly responsible for the scattering in the low-wavenumber range provided by the graphite-like vibrations of carbon atoms [54], while the above unit vibrations are the most active in the region of $350\text{-}800\text{ cm}^{-1}$ and of $750\text{-}1200\text{ cm}^{-1}$ - related to OH and CH, respectively. Yet considering the presence of CH units in the (5,5) GO molecule structure as service, their contribution from the molecule spectrum was extracted thus presenting the spectrum caused by hydroxyls located at the carbon core in Fig. 22b. The total spectrum of the $\{\text{GO}+\text{water}\}$ model - with the CH units

excluded - is shown in Fig. 22c. Fig. 22d shows the total scattering spectrum of 48 water molecules only. As seen, the latter constitutes the dominant part of the $\{\text{GO}+\text{water}\}$ -CH spectrum.

Particular attention should be given to the convolution series at each panel of Fig. 22. According to Eq. (3), the originally calculated $G(\omega)$ spectra present the extended sets of δ -functions (shown at each panel). Multiple different internal and external factors, such as finite lifetime and anharmonicity of vibrations as well as various structural and dynamic inhomogeneities, result in the broadening of the spectral shape. This is usually taken into account via convolution of the δ -spectra with Lorentzians with a different half-width. As seen in the figure, the broadening significantly affects the spectra shapes, thus, the spectra related to L20 and L100 look differently. While L20 curves may be considered as the ones of the highest level of anharmonicity and short-time living of vibrations, L100 curves disclose the inhomogeneity effects. The latter are highly expected in systems similar to the studied GO and rGO samples.

Since the water plays the main role in the INS scattering of the $\{\text{GO}+\text{water}\}$ model let us consider the water spectrum more attentively. As mentioned in Section 4.1, water molecules forming monolayers around (5,5) GO substrates are nevertheless differently coordinated in terms of the number of H-bonds, N_{HB} . As occurred, in the current model N_{HB} changes from 4 to 1, thus pointing to four-, three-, two-, and one-HB configured molecules and constitutes 7, 10, 25, and 6 (7:10:25:6 HB-composition below), respectively. It should be noted that none of the four- and three-HB molecules surrounded by other water molecules, which is a characteristic feature of free water, is observed. Evidently, the dynamics of differently configured water molecules is not the same. To reveal the difference, N_{HB} was laid into the foundation of further partitioning of the calculated INS spectra.

The left panels in Fig. 23 present the N_{HB} -partitioned spectra of water for $N_{\text{HB}} = 1, 2, 3,$ and 4 - normalized per 100% molecular fraction of each. When turning from $N_{\text{HB}} = 1$ to $N_{\text{HB}} = 4$, the spectra undergo a continuous upshifting. By comparing these spectra with the experimental $G(\omega)$ spectrum of GO at 20K presented in panel (a) of the right column of Fig. 23, one can see that differently N_{HB} -configured molecules contribute into different parts of the experimental spectrum. Both experimental and calculated water INS spectra have characteristic three regions related to hindered translations (A and L) and librations (B), described in details in

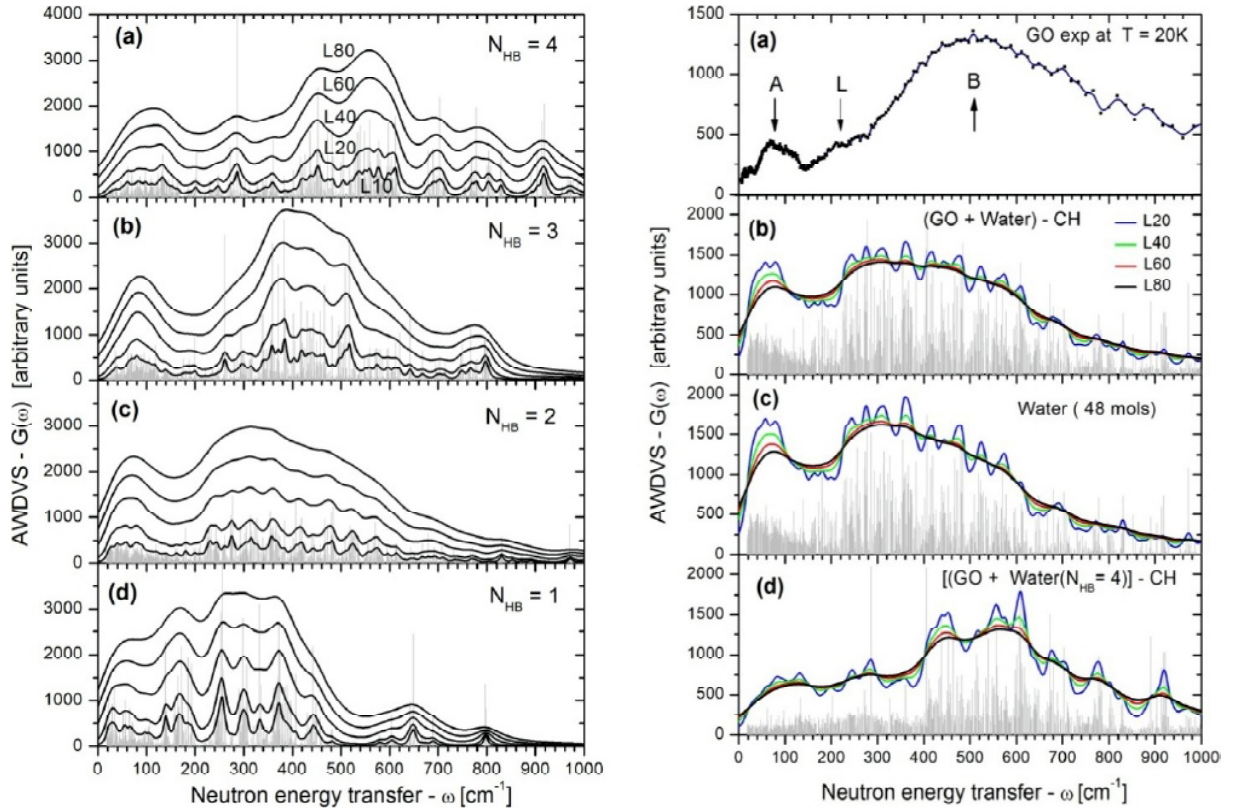


Fig. 23. AWDVS $G(\omega)$ spectra of GO. Left: N_{HB} -partitioned spectra of water molecules related to $N_{HB}=4$ (a); $N_{HB}=3$ (b); $N_{HB}=2$ (c); and $N_{HB}=1$ (d). See further details in the caption to Fig. 22. Right: (a). Experimental $G(\omega)$ spectrum of Ak-GO at 20K; (b). Total spectrum of the {GO+water} model exempted from the contribution of CH units; (c) The spectrum of involved 48 water molecules. (d) The same as in panel (b) but with $N_{HB}=4$ -configured water molecules. Different L-spectra are normalized to the same area.

Section 3.3. As for partitioned calculated spectra, those related to $N_{HB}=1$ and $N_{HB}=2$ are mainly responsible for the translational A and L parts of the real spectrum while $N_{HB}=3$ and $N_{HB}=4$ spectra are well consistent with the librational part B. Therefore, the experimental spectrum actually presents a convolution of the contributions provided with differently configured water molecules, which obviously depend on the relevant N_{HB} . In practice, the N_{HB} composition is not only difficult to be predicted, but should not be treated as a fixed, since the water substance is quite living. Consequently, it is not surprising that the calculated 7:10:25:6 N_{HB} composition of the studied {GO+water} model does not fit the experimental $G(\omega)$ spectrum of Ak-GO in details as seen in the right panels (b) and (c). However, when all the molecules are artificially substituted by the $N_{HB}=4$ -configured ones (panel (d)), fitting becomes much better, which might indicate a preferential presence of the $N_{HB}=4$ -configured molecules in the real case. The latter is more pronounced in the case of the ppGO experimental spectrum (see Fig. 14d). The dependence of the total spectrum shape on the contribution of alternatively

configured molecules may be the reason of the fact that the INS spectra of the interlayer retained water are quite similar in different matrices with respect to the general character of the shape, while the position of B band - as well as intensity of the bridging linking L - are different due to the difference in the configuration conditions. A comparison of the right panels spectra ((a) and (d) of Fig. 23) shows that not questioned inhomogeneity of the studied GO sample is rather significant and may be characterized in terms of Lorentzian's parameters by L80.

4.3. INS spectrum of rGO. Computational results and discussion

The left column of Fig. 24 presents a comparative view of the experimental sh-rGO $G(\omega)$ spectrum alongside with the calculated ones based on the (5,5) graphene hydrides CH1 and CH2. As seen in the figure, the calculated CH1 better fits the experimental sh-rGO spectrum as well as the spectrum of TEGO-H studied in [49] (see right panel (c) in Fig. 16). Calculations well reproduce slightly grow-

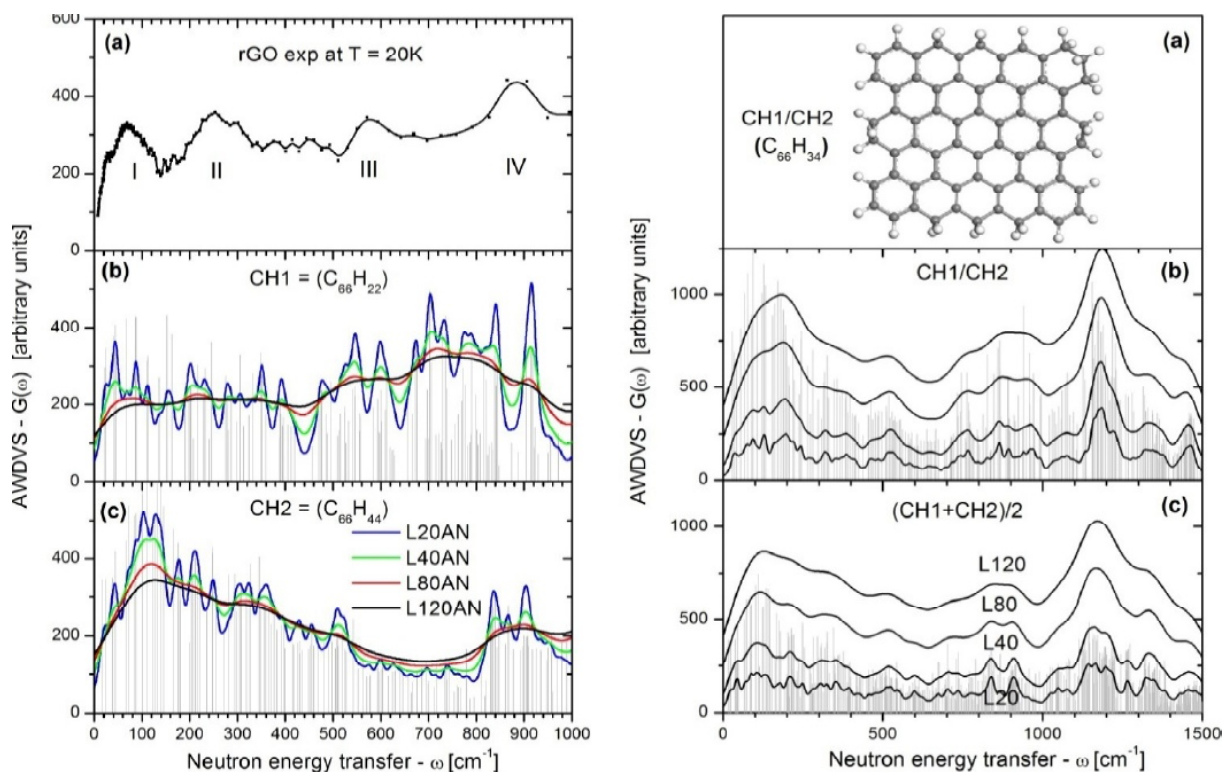


Fig. 24. AWDVS $G(\omega)$ spectra of rGO. Left: (a). Experimental $G(\omega)$ spectrum of sh-rGO at 20K; (b) and (c). Calculated $G(\omega)$ spectra (area normalized) of CH1 and CH2 models shown in Fig. 20. Right: (a) Equilibrium structure of the $C_{66}H_{34}$ molecule (hybrid CH1/CH2 model). Atoms marking see in the caption to Fig. 17. (b). Calculated $G(\omega)$ spectra of the CH1/CH2 model. (c). The halved sum of (CH1 and CH2) spectra from the right panels (b) and (c). The 0-1 IINS vibrational mode intensities (light gray bars) were convoluted by using Lorentzians of 20, 40, 80, and 120 cm^{-1} half width (black lines L20, L40, L80, and L120, respectively). The labeling is attributed to all panels.

ing intensity with gradually decreasing growth rate that is characteristic for both spectra up to ~ 500 cm^{-1} . The region is related to graphite-like modes [54] and its continuous smooth appearance is attributed to nanosize of the relevant rGO sheets. The feature can be traced also in the spectra of Ak-rGO and TErGO (left (a) and (b) panels in Fig. 16) in spite of additional structuring of the latter that might be attributed to size effects caused by submicron lateral dimensions of the rGO sheets.

In experimental spectra above 500 cm^{-1} the previous feature becomes a practically steady background above which two characteristic bands appear in region of $500-700$ cm^{-1} and $700-1000$ cm^{-1} . The bands are observed in all the studied rGOs presented in Fig. 16 and are provided with non-planar deformational vibrations of C-H bonds [49,55]. The calculated CH1 spectrum reproduces only onset of these vibrations rising over the background, small intensity of which remains a question. The substitution of CH units by CH_2 ones does not improve the result and even worsens it. At the same time, as seen in right panels (b) and (c) of Fig. 24, a mixture of CH and CH_2 units may lead to a wished ef-

fect. Both experimental spectra of different rGOs and the discussed calculated spectra show that the real chemical composition of the rGO circumference area as well as its size and shape are responsible for the variability of the relevant INS spectra as well as of other physics-chemical properties of rGOs.

As for chemical composition of different rGO sheets, it may vary, thus, contributing into the structural and content heterogeneity of the structural motifs of the studied rGO. According to the series of convolution data presented in Fig. 24, the latter can be evaluated as L100 and can be responsible for the discrepancy between the experimental and calculated spectra, since the latter is usually attributed to a specific structural and content model.

5. GO INSTABILITY REVEALED BY INS

Chemists have repeatedly testified that both GOs and rGOs are not only characterized by largely varied properties but are chemically unstable in time. Evidently, both GO and rGO molecules are chemically active due to which they might be subjected

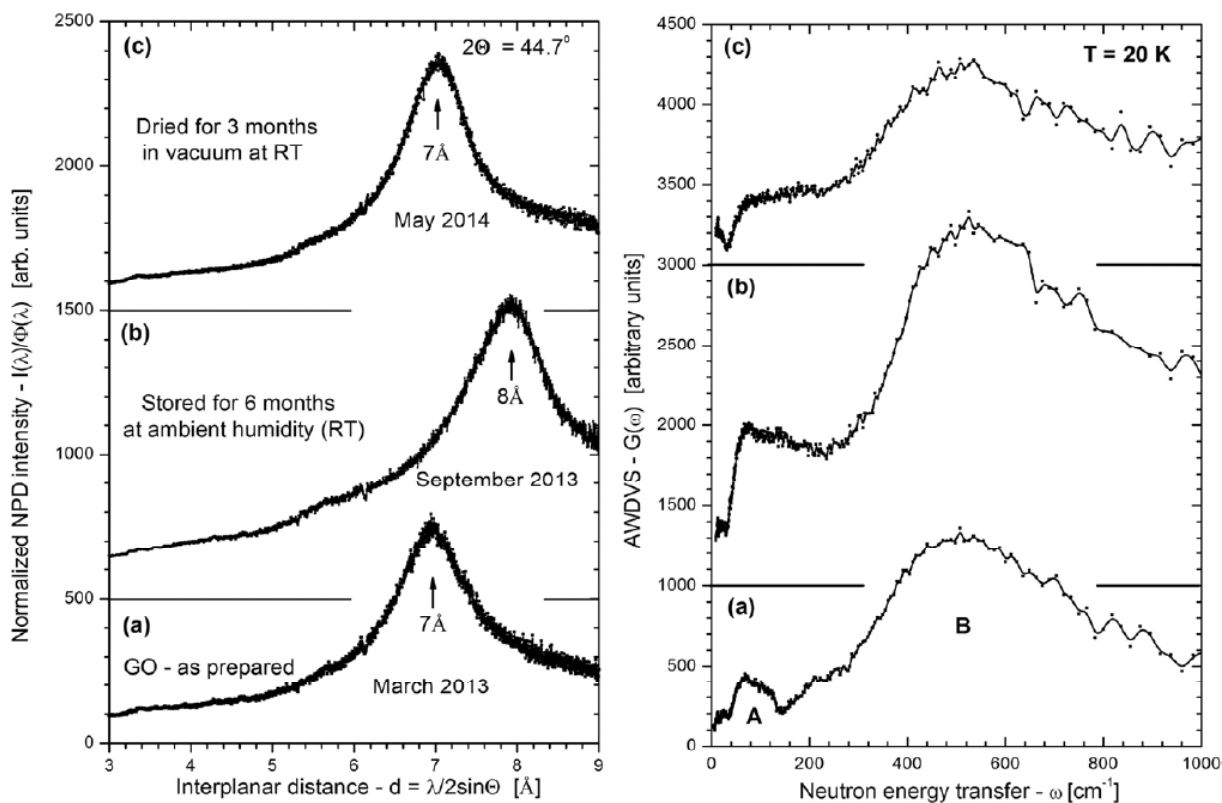


Fig. 25. The evolution of NPD patterns (left panels) and $G(\omega)$ spectra of Ak-GO at $T=20\text{K}$ (right panels) in time (see text).

to different reactions. One of such reaction concerns the interaction of GO with water. As shown by Tour and his colleagues [56], the interaction of GO with water is so strong that is right to speak about dynamic structural model (DSM) of GO: thus, GO does not contain any significant quantity of preexisting acidic functional groups, but gradually generates them through interaction with water. The reaction with water results in C-C bond cleavage, formation of vinylogous carboxylic acids, and the generation of protons. Besides, previously was shown that water surrounding was enough for the GO reduction to be able to occur [57]. It was suggested [16] that this very reaction laid the foundation of the rGO formation at natural conditions providing the appearance of shungite carbon.

Obviously, not only environmental, but retained water can act similarly due to which both the state of the retained water and the GO core structure would be expected to change in time. This is really the case, which is demonstrated in Fig. 25. The NDP fragments and INS $G(\omega)$ spectra of freshly prepared GO are shown in panels (a) of the figure. As was said earlier, the interlayer distance of 7 Å evidences the lowest content of retained water. After withstanding the sample at room temperature and ambient humidity for six months both pictures

change (see panels (b) of the figure). The NDP shows increasing the interlayer distance from 7 to 8 Å; the intensity of the $G(\omega)$ spectra practically doubles and their shape is remarkably altered. As seen in the figure, the changes affect both A and B parts of the water spectrum: the first is slightly up-shifted while the latter becomes some structured. The bridged linking L becomes less pronounced. This GO sample was afterwards kept at room temperature in a soft vacuum for three months. Panels (c) of Fig. 25 present changes that have occurred. According to NPD, the interlayer distance comes back to 7 Å albeit the diffraction peak becomes slightly broader. As for $G(\omega)$ spectrum, in spite of its intensity becomes comparable with that one in Fig. 25a, it cannot be attributed to the retained water due to significant change of the spectra shape in regions A and L. The presence of clearly seen band at $\sim 80\text{ cm}^{-1}$ and a particular form of linking are the main characteristic features of the INS spectra of water. Pronouncedly seen in Fig. 25a, they disappear in Fig. 25c while the structured character of the B region becomes more vivid.

The observation convincingly shows changes that are connected with the retained water. Keeping the sample in a considerable humidity for a long time is evidently followed with the accumulation of additional

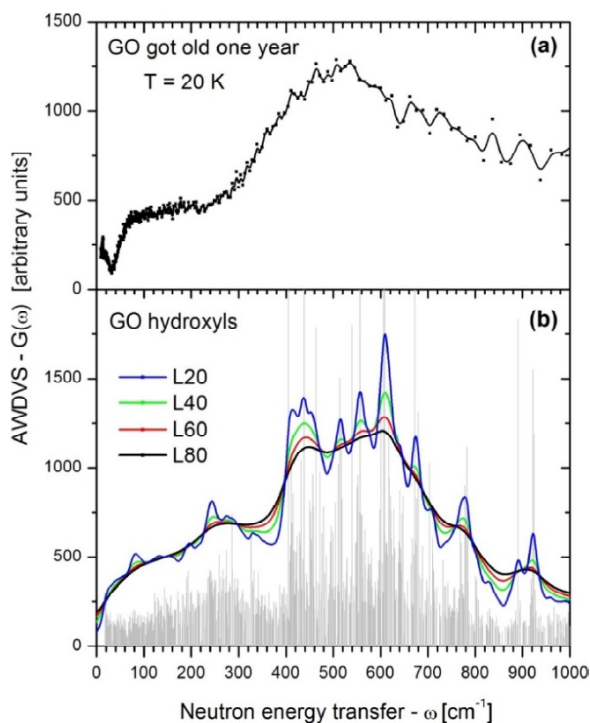


Fig. 26. (a). Time-evolved AWDVS $G(\omega)$ spectrum of Ak-GO at 20K (see text). (b). Calculated $G(\omega)$ spectrum of hydroxyls accommodated on the basal plane of the (5, 5) GO molecule.

water that penetrates into the space between the layers. Such an action is expectedly accompanied with the growth of the interlayer distance, which was earlier observed for GrO [38], as well as with increasing the scattering intensity, which is exhibited in Fig. 25b. However, attention should be given to the evident structuring of the spectrum in the B region. As shown in Fig. 22b, the main contribution to the INS scattering from hydroxyls located at the carbon substrate should occur in this very region. Since such a structure is not observed for the pristine sample in Fig. 25a, one may suspect the appearance of hydroxyls during the time. If the reaction did not occur, a long-term pumping out of the sample should have removed all the retained water causing a drastic lowering of the scattering intensity. As shown in Fig. 25c, this is not the case; the scattering intensity is comparable with that one for the pristine sample, which means that strong neutron scattering agents still remain in the sample just pointing to the hydroxyls discussed. Actually, the hydroxyl formation, which occurred in due course of water molecule dissociation in the vicinity of epoxy groups of GO, is considered as the main reason of the GO structure change resulting in the GO DSM behavior and its reduction [56,57].

Fig. 26 presents a comparative vision of the experimental and calculated spectra of hydroxyls lo-

cated at the carbon substrate shown in Fig. 22b. As seen in Fig. 26, the calculated spectrum reproduces the experimental one quite well thus confirming the retained water dissociation and the accumulation of hydroxyls located over the GO sample basal plane. Assessing agreement between the calculated and empirical data, it is necessary to bear in mind the structural and chemical heterogeneity of the parent graphene sheets in practice that evidently significantly influences the shape of experimental spectrum.

Participation of retained water in chemical reactions has been convincingly demonstrated recently in experiments on the reduction of graphene oxide employing camera flash [58] as well as on the GO job as a water dissociation catalyst in the bipolar membrane interfacial layer [59].

6. CONCLUSION

Graphene oxide and reduced graphene oxide turned out to be favorite species for neutron scattering study. Hydrophilicity of GO and hydrophobicity of rGO are responsible for intense neutron scattering in each of the cases. The former is promoted with a considerable retaining of water between individual GO sheets as well as with hydroxyls that are formed in due course of the interaction of the retained water with epoxy groups on the GO basal plane. In the second case, the degree of filling of the rGO circumference with hydrogen depends on the hardness of the reduction conditions. C-H bonds formed in due course of the reduction actively participate in scattering via excitation of vibrations - both directly connected with the bonds and involved in the vibrations of the carbon core by 'riding effect'. Combining with a superb sensitivity of neutron scattering on protium, the above features provide a large hydrogen-sensitive method. In practice, the hydrogen saturation of both GO and rGO is quite variable and dependent on chemical protocols of the species production and conditions of their storage. In view of this, neutron scattering can be considered as a reliable technique to trace changes in the products caused by some of such reasons. Thus, thanks to neutron study of shungite was able to prove that 1) shungite carbon is actually of a multilevel porous structure based on nanoscale rGO sheets; 2) individual rGO sheets present slightly oxidized FOHGs with all hydrogen and oxygen atoms located in the circumference area of the sheet leaving the sheet basal plane chemically not modified; 3) in the series of structure levels that is sheets \rightarrow sheet stacks \rightarrow globules \rightarrow agglomerates a reliable model of the

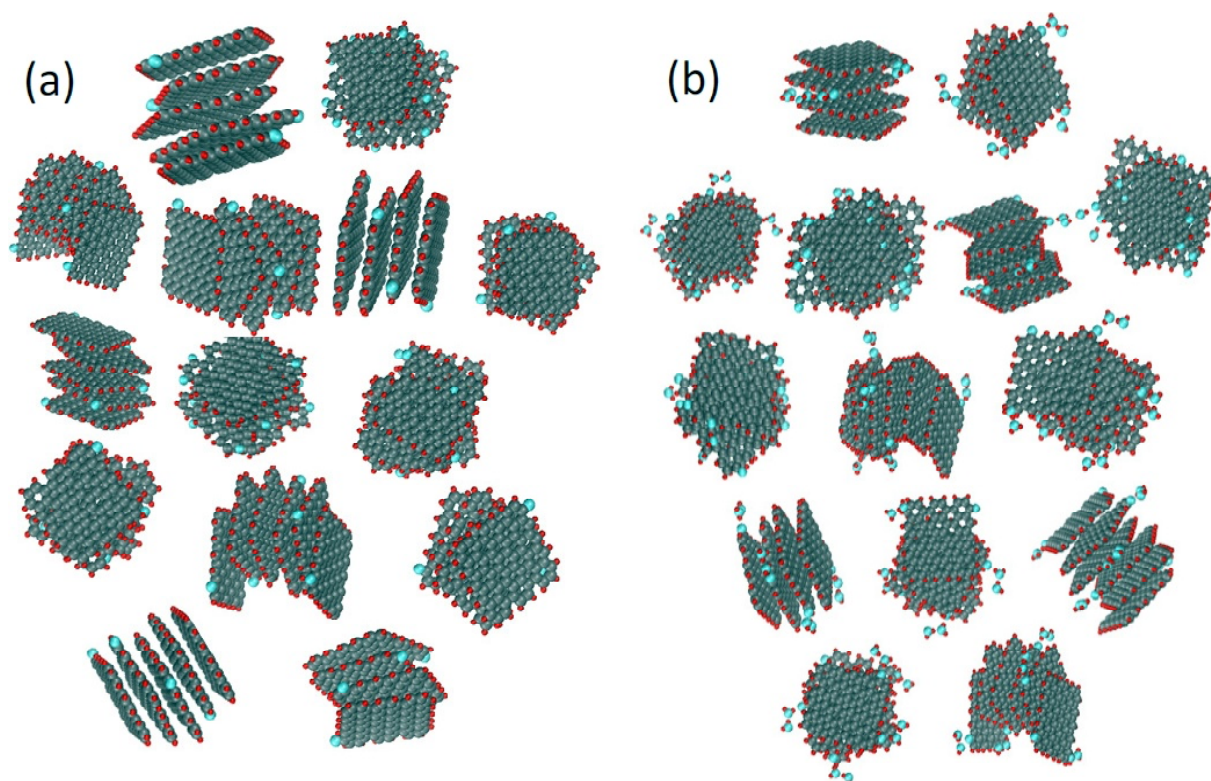


Fig. 27. Planar presentation of a model of *dry* (a) and *wet* (b) shungite carbon globules consisting of a set of four-, five- and six-layer stacks of (5, 5) rGO sheets of the $C_{66}O_1H_{21}$ chemical composition voluntarily located and oriented in space. Linear dimensions along the vertical and horizontal are of ~ 6 nm. The atom colorings see in the caption to Fig. 18.

globes can be presented with respect to both their structure and chemical composition. The models are shown in Fig. 27 for *dry* and *wet* shungite carbons. Presented in the figure are planar projections of a globe structure voluntarily packed with differently projected stacks of different sizes. The interglobe pores are compatible with linear dimensions of rGO stacks and are quite suitable for confining water. The stacks surface forms the inner surface of the pores that are carpeted with hydrogens while the only oxygen atom is shaded by two water molecules. The amount of oxygen atoms determines the quantity of water which is bound with the pore surface. Taken together, all the findings convincingly testify that shungite carbon is a natural pantry of highly important technological material that is known as technological graphene [16,20].

ACKNOWLEDGEMENTS

The authors are grateful to N.N.Rozhkova, S.P.Gubin, E.Yu.Buslaeva, S.V.Tkachev, V.P.Mel'nikov for the provision of GO and rGO products of different origin; to K. Druzbicki for providing computed $G(\omega)$ spectra; to S.Rols and C.Cavallari for supplying with the data obtained in the course of

experiments at the IN1 spectrometer at the HFR ILL as well as for kind permission to use the data at our discretion. All the mentioned colleagues are greatly appreciated for fruitful discussions of the obtained results

REFERENCES

- [1] E.F. Sheka, N.N. Rozhkova, I. Natkaniec and K. Holderna-Natkaniec // *JETP Lett.* **99** (2014) 754.
- [2] E.F. Sheka, N.N. Rozhkova, K. Hołderna-Natkaniec and I. Natkaniec // *Nanocryst: Phys. Chem. Math.* **5** (2014) 659.
- [3] I. Natkaniec, E.F. Sheka, K. Druzbicki, K. Hołderna-Natkaniec, S.P.Gubin, E.Yu. Buslaeva and S.V. Tkachev // *J. Phys. Chem. C* **119** (2016) 18650.
- [4] E.F. Sheka, I. Natkaniec, V.P. Mel'nikov, and K.Druzbicki // *Nanocryst: Phys. Chem. Math.* **6** (2015) 378.
- [5] K.S. Novoselov, V.I. Fal'ko, L. Colombo, P.R. Gellert, M.G. Schwab and K. Kim // *Nature* **490** (2012) 192.
- [6] E.F. Sheka // *Int. J. Quant. Chem.* **114** (2014) 1079.

- [7] A.C. Ferrari, F. Bonaccorso and V. Fal'ko // *Nanoscale* **7** (2015) 4598.
- [8] M. Peplow // *Nature* **503** (2013) 327.
- [9] E. Sheka and N. Popova // *Phys. Chem. Chem. Phys.* **15** (2013) 13304.
- [10] T. Kuila, S. Bose, A.K. Mishra, P. Khanra, J.N.H. Kim and H. Lee // *Progr. Mat. Sci.* **57** (2012) 1061.
- [11] J. Luo, J. Kim and J. Huang // *J. Acc Chem. Res.* **46** (2013) 2225.
- [12] C.K. Chu and M. Pumera // *Chem. Soc. Rev.* **43** (2014) 291.
- [13] J. Zhao, L. Liu and F. Li, *Graphene Oxide: Physics and Applications* (Springer, 2015).
- [14] P. V. Kumar, N. M. Bardhan, S. Tongay, J. Wu, A. M. Belcher and J. C. Grossman // *Nat. Chem.* **6** (2014) 151.
- [15] J.-Y. Hong, J. Kong and S.H. Kim // *Small* **10** (2014) 4839.
- [16] E.F. Sheka and N.N. Rozhkova // *Int. J. Smart Nano Mat.* **5** (2014) 1.
- [17] N.N. Rozhkova, *Shungite Nanocarbon* (Karelian Research Centre of RAS, Petrozavodsk, 2011), In Russian.
- [18] N.N. Rozhkova, A.V. Gribanov and M.A. Khodorkovskii // *Diamond Relat. Mater.* **16** (2007) 2104.
- [19] N.N. Rozhkova // *Russ. J. Gen. Chem.* **83** (2013) 2676.
- [20] E.F. Sheka and E.A. Golubev // *Techn. Phys.* **61** (2016), in print.
- [21] www.akkolab.ru
- [22] S.V. Tkachev, E.Yu. Buslayeva, A.V. Naumkin, S.L. Kotova, S.V. Laure and S.P. Gubin // *Inorg. Mat.* **48** (2012) 796.
- [23] W.S. Hummers and R.E. Offeman // *J. Am. Chem. Soc.* **80** (1958) 1339.
- [24] S.P. Gubin // *Doklady Chemistry* **345** (1995) 304.
- [25] D. Krishnan, F. Kim and J. Luo // *Nano Today* **7** (2012) 137.
- [26] I. Natkaniec, D. Chudoba, L. Hetmańczyk, V.Yu. Kazimirov, J.I. Krawczyk, L. Sashin and S.J. Zalewski // *J. Phys. Conf. Series* **554** (2014) 012002.
- [27] W. Marshall and S.W. Lovesey, *Theory of Thermal Neutron Scattering*, (Oxford, 1971).
- [28] K. Drużbicki and I. Natkaniec // *Chem. Phys. Lett.* **600** (2014) 106.
- [29] E.L. Bokhenkov, I. Natkaniec and E.F. Sheka // *Sov. Phys. JETP* **43** (1976) 536.
- [30] S.V. Opalev and E.A. Belenkov // *Izvestiya Chelyabinskogo Nauchnogo Centra* **3** (2004) 27, In Russian.
- [31] G.I. Emel'yanova, L.E. Gorlenko, N.N. Rozhkova, M.N. Rymyantseva and V.V. Lunin // *Russ. J. Phys. Chem. A* **84** (2010) 1376.
- [32] V.V. Kovalevski, P.R. Buseck and J.M. Cowley // *Carbon* **39** (2001) 243.
- [33] Z. Sofer, P. Šimek, O. Jankovský, D. Sedmidubský, P. Beranb and M. Pumera // *Nanoscale* **6** (2014) 13082.
- [34] S. Pan and I.A. Aksay // *ACS Nano* **5** (2011) 4073.
- [35] N. A. Nebogatikova, I. V. Antonova, V. Ya. Prinz, I. I. Kurkina, V. I. Vdovin, G.N. Aleksandrov, V. B. Timofeev, S.A. Smagulova, E. R. Zakirov and V.G. Kesler // *Phys. Chem. Chem. Phys.* **17** (2015) 13257.
- [36] A.I. Kolesnikov, E.L. Bokhenkov and E.F. Sheka // *JETP* **57** (1984) 1273.
- [37] M.R. Johnson, K. Parlinski, I. Natkaniec and S. Hudson // *Chem. Phys.* **291** (2003) 53.
- [38] A. Buchsteiner, A. Lerf and J. Pieper // *J. Phys. Chem. B* **110** (2006) 22328.
- [39] J.L. Finney // *Phil. Trans. Roy. Soc. Lond. B* **359** (2004) 1145.
- [40] V. Crupi, D. Majolino, P. Migliardo and V. Venuti // *J. Phys. Chem. B* **106** (2002) 10884.
- [41] A. I. Kolesnikov, J.-M. Zanotti, C.-K. Loong and P. Thiyagarajan // *Phys. Rev. Lett.* **93** (2004) 035503.
- [42] C. Corsaro, V. Crupi, D. Majolino, S.F. Parker, V. Venuti and U. Wanderlingh // *J. Phys. Chem. A* **110** (2006) 1190.
- [43] S.-H. Chen and C.-K. Loong // *Nucl. Eng. Techn.* **38** (2006) 201.
- [44] C.E. Bertrand, Y. Zhang and S.-H. Chen // *Phys. Chem. Chem. Phys.* **15** (2013) 721.
- [45] N.N. Rozhkova, G.I. Emel'yanova, L.E. Gorlenko, A.G. Gribanov and V.V. Lunin // *Glass Phys. Chem.* **37** (2011) 621.
- [46] M.V. Avdeev, T.V. Tropin, V.L. Aksenov, L. Rosta, V.M. Garamus and N.N. Rozhkova // *Carbon* **44** (2006) 954.
- [47] P.G. Hall, A. Pidduck and C.J. Wright // *J. Colloid. Interface Sci.* **79** (1981) 339.
- [48] E.F. Sheka, V.D. Khavryutchenko and I.V. Markichev // *Russ. Chem. Rev.* **64** (1995) 389.
- [49] C. Cavallari, D. Pontiroli, M. Jiménez-Ruiz, A. Ivanov, M. Mazzani, M. Gaboardi, M. Aramini, M. Brunelli, M. Riccò and

- S. Rols // *J. Phys. Conf. Series* **554** (2014) 012009.
- [50] C. Bousige, S. Rols, J. Cambedouzou, B. Verberck, S. Pekker, E. Kovats, G. Durkò, I. Jalsovsky, E. Pellegrini and P. Launoi // *Phys. Rev. B* **82** (2010) 195413.
- [51] E.F. Sheka // *Int. J. Quant. Chem.* **112** (2012) 3076.
- [52] E. Sheka and N. Popova // *J. Mol. Mod.* **18** (2012) 3751.
- [53] Z. Xu, Y. Bando, L. Liu, W. Wang, X. Bai and D. Golberg // *ACS Nano* **5** (2011) 4401.
- [54] R. Nicklow, N. Wakabayashi and H.G. Smith // *Phys. Rev. B* **5** (1972) 4951.
- [55] M. Margoshes and V.A. Fassel // *Spectrochimica Acta* **7** (1955-1956) 14.
- [56] A.M. Dimiev, L.B. Alemany and J.M. Tour // *ACS Nano* **7** (2013) 576.
- [57] K.-H. Liao, A. Mittal, S. Bose, C. Leighton, K.A. Mkhoyan and C.W. Macosko // *ACS Nano* **5** (2011) 1253.
- [58] S. Bose and L.T. Drzal // *Nanotechnology* **25** (2014) 075702.
- [59] M.B. McDonald and M.S. Freund // *ACS Appl Mater Interf.* **6** (2014) 13790.